

Exploring Effects in Tippers at Island Magnetic Observatories due to Realistic Depth- and Time-Varying Oceanic Electrical Conductivity

Rafael Rigaud (✉ rafael.rigaud@hotmail.com)

Observatorio Nacional <https://orcid.org/0000-0002-2299-6430>

Mikhail Kruglyakov

Institute of Geophysics, ETH Zürich

Alexey Kuvshinov

Eidgenössische Technische Hochschule Departement Umweltsystemwissenschaften

Katia Pinheiro

Observatorio Nacional

Johannes Petereit

GFZ German Research Centre for Geosciences

Juergen Matzka

GFZ German Research Centre for Geosciences

Elena Marshalko

Eidgenössische Technische Hochschule Departement Umweltsystemwissenschaften

Full paper

Keywords: Ocean induction effect, tippers, 3-D electromagnetic modeling, island geomagnetic observatories, oceanic 32 electrical conductivity

Posted Date: May 8th, 2020

DOI: <https://doi.org/10.21203/rs.3.rs-26496/v1>

License: © ⓘ This work is licensed under a Creative Commons Attribution 4.0 International License.

[Read Full License](#)

1 **Exploring Effects in Tippers at Island Magnetic Observatories**
2 **due to Realistic Depth- and Time-Varying Oceanic Electrical**
3 **Conductivity**

4 Rafael Rigaud^{1*}, Mikhail Kruglyakov^{2,3}, Alexey Kuvshinov², Katia Pinheiro¹, Johannes
Petereit⁴, Juergen Matzka⁴ and Elena Marshalko^{2,5,6}

*Correspondence: rafael.rigaud@hotmail.com

6 **Abstract**

7 Geomagnetic observatories around the world continuously measure time variations of the geomagnetic
8 field. Long-period (> 3 hours) variations are traditionally used to constrain the electrical conductivity
9 of the Earth's mantle either in terms of one-dimensional (1-D) or three-dimensional (3-D) conductivity
10 distributions. Recent studies have also shown that vertical transfer functions (tippers) estimated from
11 short-period (< 3 hours) variations at island observatories can constrain the 1-D conductivity
12 distribution of the oceanic lithosphere and upper mantle. This is feasible due to the
13 bathymetry-dependent ocean induction effect (OIE), which originates from lateral conductivity
14 contrasts between ocean and land and leads to non-zero tippers even for 1-D conductivity distributions
15 below the ocean. Thus, proper analysis of island tippers requires accurate 3-D modeling of the OIE, for
16 which so far was performed assuming constant sea water electric conductivity with depth. However,
17 significant changes of electric conductivity with depth in the top hundreds of meters of the water
18 column do occur. In this study we explore – using rigorous 3-D electromagnetic (EM) modeling – to
19 what extent realistic, depth-dependent, oceanic conductivity affects island tippers. The modeling is
20 performed for 10 island observatories around the world in the period range 10^{-1} to 10^4 seconds, for
21 which a perceptible OIE on tippers is expected. We then compare the predicted tippers with tippers
22 estimated from the observatory data. We also investigate, again using 3-D EM modeling, the effect of
23 seasonal variations of the oceanic conductivity and to which extent this could explain the observed
24 systematic seasonal variation of tippers. We find good agreement between predicted and estimated
25 tippers for all 10 island observatories. This confirms that tippers at island observatories are mainly
26 influenced by the bathymetry-dependent OIE. Our model studies suggest that for most of the considered
27 island observatories, the effect from depth-varying oceanic conductivity is tangible and exceeds the
28 error floor of 0.025, which usually is assigned to tippers during their inversion. Contrarily, the effects
29 from seasonally varying oceanic conductivity were found to be too small to be worth consideration.

30 **Keywords**

31 Ocean induction effect, tippers, 3-D electromagnetic modeling, island geomagnetic observatories, oceanic
32 electrical conductivity

33 **Introduction**

34 One of the geophysical methods to probe the physical parameters of the Earth’s mantle is Geomagnetic
35 Depth Sounding (GDS; Banks, 1969; Weidelt, 1972). GDS exploits magnetic field variations of magneto-
36 spheric and/or ionospheric origin and allows to constrain electrical conductivity at depth. The main data
37 source for GDS are magnetic field measurements performed at the global net of geomagnetic observato-
38 ries. Long-period (> 3 hours) variations are routinely used in GDS to constrain electrical conductivity
39 of the Earth’s mantle either in terms of local one-dimensional (i.e. vertical, 1-D; Olsen, 1998; Utada
40 et al, 2003; Munch et al, 2018, among others) or three-dimensional (3-D; Kelbert et al, 2009; Semenov
41 and Kuvshinov, 2012; Koyama et al, 2014; Sun et al, 2015, among others) conductivity distributions.
42 Recent studies (Samrock and Kuvshinov, 2013; Morschhauser et al, 2019) have also shown that vertical
43 transfer functions (tippers) estimated from short-period (< 3 hours) variations at island observatories
44 can be used to constrain 1-D conductivity distributions of the oceanic lithosphere and upper mantle.
45 This becomes feasible due to the ocean induction effect (OIE; cf. Parkinson and Jones, 1979), which
46 originates from the lateral conductivity contrast between ocean and land. The OIE leads to non-zero
47 tippers even for 1-D conductivity distribution beneath the ocean (cf. Samrock and Kuvshinov, 2013).
48 The interpretation of island tippers requires accurate 3-D electromagnetic (EM) modeling of the OIE
49 that takes into account the bathymetry around the observatory. So far, these models assumed constant
50 oceanic electric conductivity with depth (cf. Samrock and Kuvshinov, 2013; Morschhauser et al, 2019).
51 In many regions of the world, however, the oceanic conductivity varies significantly within the uppermost
52 few hundred meters of the water column (cf. Tyler et al, 2017). In this study, we explore the extent to
53 which realistic depth-varying oceanic conductivity affects island tippers. Our analysis is performed for
54 10 island observatories located in the Pacific, Atlantic and Indian Ocean (cf. Figure 1). In addition, we
55 investigate the effect of seasonal variations of oceanic conductivity and to which extent this could explain
56 the systematic seasonal variations in tippers showed by Araya Vargas and Ritter (2016) and attributed
57 to the variability of external magnetic source fields.

58 **Methods**

59 **Tippers**

60 In non-polar regions, the source of the magnetic field variations with periods shorter than 3 hours is
61 well approximated by a vertically incident plane wave. The plane wave assumption allows one to

62 relate the vertical component B_z with the horizontal component $\mathbf{B}_H = (B_x \ B_y)$ via the so-called tipper
 63 $\mathbf{T} = (T_{zx} \ T_{zy})$ (Berdichevsky and Dmitriev, 2008)

$$B_z(\omega, \mathbf{r}) = T_{zx}(\omega, \mathbf{r})B_x(\omega, \mathbf{r}) + T_{zy}(\omega, \mathbf{r})B_y(\omega, \mathbf{r}), \quad (1)$$

64 where $\omega = 2\pi/P$ is the angular frequency of magnetic field variations with period P . The x - and
 65 y -directions are defined in this paper as the directions to geographic North and East, respectively, and
 66 z is vertically downwards. As a consequence of the plane-wave excitation, B_z (and thus \mathbf{T}) are nonzero
 67 only above non-1-D conductivity structures. In fact, one can interpret \mathbf{T} as a measure of the tipping of
 68 the magnetic field out of the horizontal plane above 2-D or/and 3-D conductivity structures.

69 **Global oceanic conductivity model**

70 The global oceanic electric conductivity model used here is that by Petereit et al (2019), which is based
 71 on the Coriolis Oceanographic data set for Re-Analysis (CORA5.0, Cabanes et al, 2013) provided by
 72 the Copernicus Marine Environment Monitoring Service. The model consists of monthly 3-D oceanic
 73 electrical conductivity distributions for 1990 to 2016. The conductivity is computed on a lateral grid of
 74 $0.5^\circ \times 0.5^\circ$ resolution and at 152 vertical levels between the sea surface and 2000 m. More details on
 75 the oceanographic data set and the calculation of the global oceanic conductivity model can be found
 76 in Petereit et al (2019). From 2000 m to the ocean bottom the sea water conductivity was set to 3.2
 77 S/m (cf. Tyler et al, 2017). As an example, Figure 2 presents global maps of the depth-averaged oceanic
 78 conductivity for a number of depth intervals for December 2015, illustrating the fact that the oceanic
 79 conductivity indeed varies with depths and laterally.

80 **Constructing 3-D conductivity models around island observatories**

81 The (Cartesian) 3-D conductivity models were constructed separately for each observatory. The models
 82 include a nonuniform oceanic bathymetry and a landmass with a uniform conductivity of 0.01 S/m. The
 83 latter is defined here as the upper crust from the surface down to the maximum depth of the ocean in the
 84 considered region. The landmass and the ocean comprise the 3-D part of the model, which is underlain by
 85 a crust and mantle with the 1-D conductivity distribution (cf. Figure 3) by Grayver et al (2017). Their
 86 1-D model was obtained by joint inversion of satellite-detected tidal and magnetospheric signals and is
 87 believed to represent the globally averaged 1-D conductivity profile beneath the oceans. More details on
 88 our models are as follows. First, we note that as far as we exploit integral equation (IE) approach to
 89 calculate the EM fields (to be discussed in the next section), the modeling domain is confined to the 3-D

90 part of the model. The vertical size of the domain corresponds to the maximum depth of the ocean in
91 the region of interest, elevations above sea level are ignored. The lateral cross-section of the 3-D volume
92 is a square of $356 \times 356 \text{ km}^2$ with the island observatory in its center. The 3-D part of the models is
93 constructed using bathymetry data from the National Oceanic and Atmospheric Administration (NOAA)
94 ETOPO1 Global Relief Model (Amante and Eakins, 2009), which is provided in spherical coordinates
95 with a lateral resolution of 1 arc min, corresponding to 1.86 km at the equator. Note that in the vicinity
96 of the GAN observatory the NOAA bathymetry model appeared to be not accurate enough, and we
97 used data from the General Bathymetry Chart of the Oceans (GEBCO, 2019), which has a 15 arc sec
98 horizontal resolution (0.46 km at the equator). Bathymetry was converted to Cartesian coordinates by
99 the use of the Transverse Mercator map projection and then linearly interpolated to a regular grid with
100 1 km horizontal resolution.

101 The uppermost left panel in Figures 5-14 shows the bathymetry in the vicinity of the considered island
102 observatory. Vertically, the 3-D modeling domain was discretized by ten 100 m thick layers from the
103 surface down to 1000 m depth; from 1000 m down to the maximum bathymetry in the region, the
104 domain was discretized by 500 m thick layers (see Figure 4). Oceanic conductivity within each vertical
105 layer is assumed to be constant and is set to the 3-D average value of the 2015 December (or June)
106 oceanic conductivity model for the layer's volume. The models from 2015 year are chosen since most of
107 experimental tippers are derived from the data for this year (or adjacent years).

108 Outside the 3-D volume, at depths between the surface and maximum depth of the ocean, conductivity
109 is assumed to be laterally-uniform (1-D) and is set to the same oceanic conductivity profile as inside
110 the volume, underlain by the 1-D model for crust and mantle. The uppermost right panel in Figures
111 5-14 depicts the vertical profile of oceanic conductivity (in purple), calculated by horizontally averaging
112 oceanic conductivity (Figure 2) in a $5^\circ \times 5^\circ$ region centered at the considered island observatory. It shows
113 that the oceanic conductivity varies significantly with depth down to approximately 1 km depth. Below
114 this depth, the values are close to 3.2 S/m. This is our model for the depth-varying ocean conductivity.
115 Furthermore, for each observatory we construct a 3-D model with a constant oceanic conductivity of
116 3.2 S/m in all vertical layers. Note that such a model was used in previous studies (cf. Samrock and
117 Kuvshinov, 2013; Morschhauser et al, 2019) to analyze island tippers. Outside the 3-D volume, the
118 oceanic conductivity is set to 3.2 S/m, underlain by the 1-D model for crust and mantle. This is our
119 model for the depth-constant ocean conductivity.

120 **3-D EM modeling**

121 To compute magnetic fields in 3-D conductivity models, we solve Maxwell's equations numerically, which,
122 in the frequency domain, are written as

$$\frac{1}{\mu_0} \nabla \times \mathbf{B}(\omega, \mathbf{r}) = \sigma(\mathbf{r})\mathbf{E}(\omega, \mathbf{r}) + \mathbf{j}^{ext}(\omega, \mathbf{r}) \quad (2)$$

123

$$\nabla \times \mathbf{E}(\omega, \mathbf{r}) = -i\omega\mathbf{B}(\omega, \mathbf{r}), \quad (3)$$

124 where $\mathbf{E}(\omega, \mathbf{r})$, $\mathbf{B}(\omega, \mathbf{r})$ and $\mathbf{j}^{ext}(\omega, \mathbf{r})$ are the position- and frequency-dependent electric and magnetic
125 fields and extraneous current density, respectively, $\mathbf{r} = (x, y, z)$, μ_0 the magnetic permeability of free
126 space, and σ the conductivity of the medium where the EM field propagates. Displacement currents are
127 ignored in the considered period range.

128 We compute magnetic fields using the 3-D EM forward modelling solver PGIEM2G (Kruglyakov and
129 Kuvshinov, 2018), which is based on a volume integral equation method with contracting kernel (Pankra-
130 tov et al, 1995; Singer, 1995). PGIEM2G supports massive parallelization and the use of a high-order
131 polynomial basis. However, in this study we exploit a piece-wise representation of the fields for the sake
132 of computational efficiency. We compute magnetic fields and then tippers at 25 periods spanning the
133 range from 0.1 to 10^4 seconds.

134 **Estimating observed responses**

135 We estimated tippers at eight INTERMAGNET island geomagnetic observatories using definite minute-
136 mean data (time series of three components of magnetic field). In addition, we estimated tippers at two
137 non-INTERMAGNET island observatories: St. Helena (SHE) and Santa-Maria/Azores (SMA), also using
138 minute-mean data. Prior to the tipper estimation, obvious spikes were removed from the corresponding
139 time series. Table 1 summarizes information about the observatories, including the time interval used for
140 the tipper estimation. This interval varies from observatory to observatory and was selected – based on
141 a trial and error approach – to obtain smooth (with respect to period) tippers with low uncertainties.
142 For each period, data were split into overlapping tapered windows of two periods length. Data in these
143 windows were Fourier transformed, giving the spectrum of the corresponding component from 300 to 9600
144 seconds. Tippers and their uncertainties were then estimated using a robust, section-averaging (Olsen,
145 1998) linear regression scheme based on the Huber norm (e.g. Aster et al, 2005; Püthe and Kuvshinov,
146 2014).

147 **Results**

148 **Effect of depth-varying oceanic conductivity**

149 Modeling results for all 10 island geomagnetic observatories are presented in Figures 5 to 14. In
150 all figures, panel (a) shows the bathymetry map with the corresponding observatory located in the
151 centre. The dashed line indicates the west-east running bathymetry profile shown in panel (b). Panel
152 (c) shows the regional depth-varying oceanic conductivity down to 2000 m (purple solid line) and the
153 constant reference oceanic conductivity (3.2 S/m, dashed orange line). Panels (d) to (g) present the
154 $\text{Re } T_{zx}$, $\text{Re } T_{zy}$, $\text{Im } T_{zx}$ and $\text{Im } T_{zy}$ tipper components, respectively. Red and orange curves correspond to
155 tippers calculated in the models with depth-varying and depth-constant oceanic electrical conductivity,
156 respectively. The blue curves represent observed tippers and their uncertainties estimated from the data.
157 One can see that both observed and modeled tippers fulfill the property (Marcuello et al, 2005) that is
158 often used as a plausibility check for estimated (observed) and predicted (modeled) tippers, namely, at
159 periods where the real part of the tipper components T_{zx} or T_{zy} reaches a maximum (or a minimum)
160 value, the corresponding imaginary part changes sign.

161 Three observations can be made immediately from panels (d)-(g) that are independent of modelling being
162 done with depth-varying or depth-constant oceanic conductivity:

163 (1) The manifestation of the OIE in the modeled tippers varies from observatory to observatory. This
164 variability of the OIE is expected to be due to the different bathymetry distributions around the islands.

165 (2) Modeled and experimental tippers agree well for all observatories, for the full spectrum from 300 to
166 9600 seconds, for both components and for both the real and imaginary part. This, in particular, means
167 that the OIE is the main player making island tippers non-zero. Any remaining discrepancy can most
168 probably be attributed to regional deviations of the crustal and mantle conductivity structure from the
169 global 1-D conductivity structure used for modeling.

170 (3) The modeled OIE in tippers can be traced to periods as short as 0.2 seconds. Here, we consider the
171 OIE as significant if it exceeds a value of 0.025, which is traditionally used as an error floor in tipper
172 inversions. (e.g. Morschhauser et al, 2019; Yang et al, 2015; Tietze and Ritter, 2013; Rao et al, 2014;
173 Bedrosian and Feucht, 2014). For HON and SMA we find $\text{Im } T_{zx}$ to exceed 0.025 at 0.2 seconds. The
174 maximum amplitude of the OIE is observed at HON observatory (cf. Figure 9), where it reaches the
175 value of 1.1 in the real part of T_{zx} at a period of 20 sec.

176 Figures 5-14, panels (h) and (i) show the effect of depth-varying oceanic conductivity on island tippers.

177 This effect is assessed by the following difference

$$\Delta T_{zi} = \sqrt{(\text{Re } T_{zi}^v - \text{Re } T_{zi}^c)^2 + (\text{Im } T_{zi}^v - \text{Im } T_{zi}^c)^2} \quad (4)$$

178 where $i \in [x, y]$, and superscripts “ v ” and “ c ” correspond to the tippers calculated in the models with
 179 depth-varying and depth-constant oceanic conductivity, respectively. The horizontal dashed line depicts
 180 the threshold value of 0.025 discussed above. As seen from Figures 5-14, the effect is notable and exceeds
 181 the threshold of 0.025 for all observatories (albeit very small in ASC, IPM and SHE). At GAN and HON,
 182 the effect is considerable, reaching values close to 0.1. On the whole, the effect becomes less pronounced
 183 at the longest considered periods.

184 The manifestation of the depth-varying oceanic conductivity in the tipper components and the period
 185 range varies from observatory to observatory. This variability, like the variability of OIE itself, is expected
 186 from the different bathymetry distributions around the islands.

187 **Effects of time-varying oceanic conductivity**

188 Figure 15 presents global maps of differences between December and June (depth-averaged) oceanic
 189 conductivity in the same depth intervals as in Figure 2. As expected, the difference varies laterally, it
 190 is the largest at shallower depths (reaching 20 percent of the mean value of oceanic conductivity) and
 191 decreases with depth.

192 Finally, we modeled the effect of time-varying oceanic conductivity on island tippers. The effect is assessed
 193 by analyzing the difference

$$\widehat{\Delta T}_{zi} = \sqrt{(\text{Re } T_{zi}^D - \text{Re } T_{zi}^J)^2 + (\text{Im } T_{zi}^D - \text{Im } T_{zi}^J)^2} \quad (5)$$

194 where $i \in [x, y]$ and superscripts “ D ” and “ J ” correspond to December and June results. For experimental
 195 tippers, December and June results stand for tippers, estimated from observatory data of corresponding
 196 2015 months. As for modeled tippers, these results mean tippers calculated in 3-D models with depth-
 197 varying oceanic conductivity models for 2015 December and June months.

198 Figures 16 and 17 demonstrate ΔT_{zx} and ΔT_{zy} at ten considered observatories as filled circles on a
 199 global map. “Experimental” and “modeled” differences are colored by light and dark blue, respectively.
 200 It is clearly seen that the effect due to time-varying oceanic conductivity is negligible.

201 It is interesting to note that the temporal variability of the experimental tippers increases with period,
202 and overall it is larger in T_{zy} .

203 **Conclusions**

204 In this study we performed the first ever analysis of the effects of realistic depth- and time-varying oceanic
205 electrical conductivity on island tippers. The analysis is based on 3-D EM modeling, which was carried
206 out for ten island observatories located in the Pacific, Atlantic and Indian Oceans. The conductivity
207 models specific for each observatory were constructed using bathymetry data (ETOPO or GEBCO) and
208 a 3-D, time-dependent global model of oceanic conductivity (Petereit et al, 2019). The Cartesian EM
209 forward solver by Kruglyakov and Kuvshinov (2018) was used for EM modeling. Modeling was performed
210 in period range ($10^{-1} - 10^4$ sec), where tippers are expected to be perceptible due to the ocean induction
211 effect.

212 The effect due to depth-varying oceanic conductivity was assessed by comparing the tippers obtained
213 from the depth-varying and depth-constant oceanic conductivity models. Our model studies show that
214 in most considered observatories (except ASC, IPM and SHE) the effect is tangible. It exceeds the error
215 floor of 0.025 which is usually assigned to tippers during their 2-D or 3-D inversion and reaches large
216 values of around 0.1 for the HON and GAN observatories. The appearance of the effect with respect
217 to period and its strength varies from observatory to observatory. Such lateral variability of the effect
218 is most probably due to different bathymetry distributions around the islands. Based on our modeling
219 results, we recommend to use depth-varying oceanic conductivity when modeling island tippers, provided
220 these data are available and trustworthy. On the contrary, the modeled effects from time-varying oceanic
221 conductivity appeared to be too small to explain the observed seasonal variations in tippers.

222 **List of abbreviations**

223 EM: Electromagnetic;

224 1-D: one-dimensional;

225 2-D: two-dimensional;

226 3-D: three-dimensional;

227 OIE: Ocean Induction Effect;

228 NOAA: National Oceanic and Atmospheric Administration;

229 GEBCO: General Bathymetry Chart of the Oceans;

230 MT: Magnetotellurics;

231 **Authors' contributions**

232 RR estimated tippers from observatory data, prepared 3-D conductivity models, performed 3-D EM
233 modeling and analyzed the results. MK provided the 3-D EM modeling code PGIEM2G and assisted
234 RR with the modeling. EM and MK provided the codes for converting global bathymetry and ocean
235 conductivity data into 3-D conductivity models. AK created the concept of the study, and AK and KP
236 supervised the RR's work. JP prepared global oceanic conductivity data. JM obtained and provided
237 SHE and SMA magnetic field data. RR drafted the manuscript, and all authors read and approved the
238 final version.

239 **Authors' information**

240 ¹: Department of Geophysics, Observatório Nacional, Rio de Janeiro, Brazil. ²: Institute of Geophysics,
241 ETH Zürich, Zürich, Switzerland. ³: Geoelectromagnetic Research Center, Institute of Physics of the
242 Earth, Troitsk, Russia. ⁴: GFZ German Research Centre for Geosciences, Potsdam, Germany. ⁵: Institute
243 of Physics of the Earth, Moscow, Russia. ⁶: Geophysical Center, Moscow, Russia.

244 **Acknowledgments**

245 The authors acknowledge national institutes around the world that operate geomagnetic observatories,
246 and INTERMAGNET (www.intermagnet.org) which promotes high standards of observatory practice.
247 We also acknowledge the work of GEBCO and NOAA groups for providing publicly available global
248 bathymetry data.

249 **Availability of data and materials**

250 The results presented in this paper rely on 1 Hz data collected at geomagnetic observatories. These
251 data were digitally filtered to produce one minute means that are available from the INTERMAGNET
252 data repository.

253 **Competing interests**

254 The authors declare that they have no competing interests.

255 **Funding**

256 RR was supported by CNPq, Process 133345/2018-1. MK was supported by grant 20-05-00001 from the
257 Russian Foundation for Basic Research. AK was partially supported by the European Space Agency
258 through the Swarm DISC project. KP was supported by FAPERJ (Jovem Cientista do Nosso Estado,
259 Process 202.748/2019). EM was supported by grant 16-17-00121 from the Russian Science Foundation.
260 JP was supported by the German Research Foundation's priority program 1788 Dynamic Earth.

261 **References**

- 262 Amante C., Eakins B. W. (2009) Etopo1 1 arc-minute global relief model: Procedures, data sources and
263 analysis. noaa technical memorandum nesdis ngdc-24. national geophysical data center, noaa.
264 doi:107289/V5C8276M
- 265 Araya Vargas J., Ritter O. (2016) Source effects in mid-latitude geomagnetic transfer functions.
266 *Geophysics Journal International* 204(1):606–630
- 267 Aster R., Borchers B., Thurber C. (2005) *Parameter estimation and inverse problems*. Elsevier
268 Academic Press, Waltham(MA)
- 269 Banks R. J. (1969) Geomagnetic variations and the electrical conductivity of the upper mantle.
270 *Geophysics Journal International* 17(5):457–487
- 271 Bedrosian P. A., Feucht D. W. (2014) Structure and tectonics of the northwestern united states from
272 earthscope usarray magnetotelluric data. *Earth Planet Sci Lett* 402:275–289
- 273 Berdichevsky M. N., Dmitriev V. (2008) *Models and methods of magnetotellurics*. Springer, Berlin
- 274 Cabanes C., Grouazel A., von Schuckmann K., Hamon M., Turpin V., Coatanoan C. (2013) The cora
275 dataset: Validation and diagnostics of in-situ ocean temperature and salinity measurements. *Ocean*
276 *Science* 9(1):1–18
- 277 GEBCO (2019) Gebco compilation group (2019) gebco 2019 grid.
278 doi:105285/836f016a-33be-6ddc-e053-6c86abc0788e
- 279 Grayver A. V., Munch F. D., Kuvshinov A. V., Khan A., Sabaka T. J., Tøffner-Clausen L. (2017) Joint
280 inversion of satellite-detected tidal and magnetospheric signals constrains electrical conductivity and

281 water content of the upper mantle and transition zone. *Geophysical Research Letters*
282 44(12):6074–6081

283 Kelbert A., Schultz A., Egbert G. (2009) Global electromagnetic induction constraints on
284 transition-zone water content variations. *Nature* 460:1003–1007

285 Koyama T., Khan A., Kuvshinov A. (2014) Three-dimensional electrical conductivity structure beneath
286 Australia from inversion of geomagnetic observatory data: evidence for lateral variations in
287 transition-zone temperature, water content and melt. *Geophys J Int* 196:1330–1350,
288 DOI 10.1093/gji/ggt455

289 Kruglyakov M., Kuvshinov A. (2018) Using high-order polynomial basis in 3-d em forward modeling
290 based on volume integral equation method. *Geophys J Int* 213:1387–1401

291 Marcuello A., Queralt P., Ledo J. (2005) Applications of dispersion relations to the geomagnetic
292 transfer function. *Physics of the Earth and Planetary Interiors* 150:85–91

293 Morschhauser A., Grayver A. V., Kuvshinov A. V., Samrock F., Matzka J. (2019) Tippers at island
294 geomagnetic observatories constrain electrical conductivity of oceanic lithosphere and upper mantle.
295 *Earth, Planets and Space* 71(1):17

296 Munch F. D., Grayver A. V., Kuvshinov A., Khan A. (2018) Stochastic inversion of geomagnetic
297 observatory data including rigorous treatment of the ocean induction effects with implications for
298 transition zone water content and thermal structure. *Journal of Geophysical Research* 123:31–51

299 Olsen N. (1998) The electrical conductivity of the mantle beneath europe derived from c-responses from
300 3 to 720 hr. *Geophys J Int* 133(2):298–308

301 Pankratov O., Avdeev D., Kuvshinov A. (1995) Electromagnetic field scattering in a heterogeneous
302 earth: A solution to the forward problem. *Izvestiya, Physics of the Solid Earth* 31(3):201–209

303 Parkinson W., Jones F. W. (1979) The geomagnetic coast effect. *Reviews of Geophysics and Space*
304 *Physics* 17(8):1999–2017

305 Petereit J., Saynisch-Wagner J., Irrgang C., Thomas M. (2019) Analysis of ocean-tide induced magnetic
306 fields derived from oceanic in situ observations: Climate trends and the remarkable sensitivity of shelf
307 regions. *Journal of Geophysical Research: Oceans* 124:8257–8270

308 Pütke C., Kuvshinov A. (2014) Mapping 3-d mantle electrical conductivity from space: a new 3-d
309 inversion scheme based on analysis of matrix q-responses. *Geophysical Journal International*
310 197(2):768–784

311 Rao C. K., Jones A. G., Moorkamp M., Weckmann U. (2014) Implications for the lithospheric geometry
312 of the iapetus suture beneath ireland based on electrical resistivity models from deep-probing
313 magnetotellurics. *Geophys J Int* 198:737759

314 Samrock F., Kuvshinov A. (2013) Tipper at island observatories: Can we use them to probe electrical
315 conductivity of the earth's crust and upper mantle? *Geophysical Research Letters* 40:824–828

316 Semenov A., Kuvshinov A. (2012) Global 3-D imaging of mantle electrical conductivity based on
317 inversion of observatory C-responses – II. Data analysis and results. 191:965–992

318 Singer B. (1995) Method for solution of maxwell's equations in non-uniform media. *Geophysical Journal*
319 *International* 120:590–598

320 Sun J., Kelbert A., Egbert G. D. (2015) Ionospheric current source modeling and global geomagnetic
321 induction using ground geomagnetic observatory data. *J Geophys Res Solid Earth* 120:67716796,
322 DOI 10.1002/2015JB012063

323 Tietze K., Ritter O. (2013) Three-dimensional magnetotelluric inversion in practicethe electrical
324 conductivity structure of the san andreas fault in central california. *Geophys J Int* 195:130147

325 Tyler R. H., Boyer T. P., Minami T., Zweng M. M., Reagan J. R. (2017) Electrical conductivity of the
326 global ocean. *Earth, Planets and Space* 69:156–166

327 Utada H., Koyama T., Shimizu H., Chave A. D. (2003) A semi-global reference model for electrical
328 conductivity in the mid-mantle beneath the north pacific region. *Geophysical Research Letters*
329 30(4):1194–1198

330 Weidelt P. (1972) The inverse problem of geomagnetic induction, z. *Geophysics* 38:257–289

331 Yang B., Egbert G. D., Kelbert A., N. M. (2015) Three-dimensional electrical resistivity of the
332 north-central usa from earthscope long period magnetotelluric data. *Earth Planet Sci Lett* 422:87–93

Table 1. : Information on the geomagnetic observatories used in this study. From left to right: IAGA code, observatory name, geographic and geomagnetic latitude and longitude, starting date of INTERMAGNET participation, and time interval used to estimate tippers. Observatories with an asterisk (*) are, as of date, not participating in INTERMAGNET and data is available from GFZ Potsdam. Geomagnetic coordinates were calculated using the IGRF-12 model, epoch 2015

Code	Name	lat^{GG}	lon^{GG}	lat^{GM}	lon^{GM}	Starting date (INTERMAGNET)	Time interval used for tippers' estimation
ASC	Ascension Island	7.95	-14.38	-2.77	57.48	2003	01/01/2014 – 31/12/2014
CKI	Cocos-Keeling Islands	12.10	-96.84	-21.56	168.92	2013	01/01/2015 – 30/06/2015
GAN	Gan	0.69	73.15	-8.64	145.33	2013	01/01/2017 – 31/12/2017
GUA	Guam	13.59	144.87	5.8	216.51	1991	01/01/2016 – 31/12/2016
HON	Honolulu	20.32	-158	21.65	270.85	1991	01/01/2015 – 30/09/2015
IPM	Easter Island	-27.2	-109.42	-19.17	325.61	2010	01/01/2013 – 31/12/2013
PPT	Pamatai	-17.57	-149.58	-15.05	285.79	1991	01/01/2015 – 31/12/2015
SHE	St. Helena	-15.96	-5.75	11.78	64.24	2009*	01/01/2013 – 30/06/2013
SMA	Santa Maria/Azores	36.99	-25.13	43.21	53.57	2018*	01/07/2018 – 31/10/2018
TDC	Trista da Cunha	-37.07	-12.31	-31.70	54.76	2010	01/01/2015 – 30/09/2015

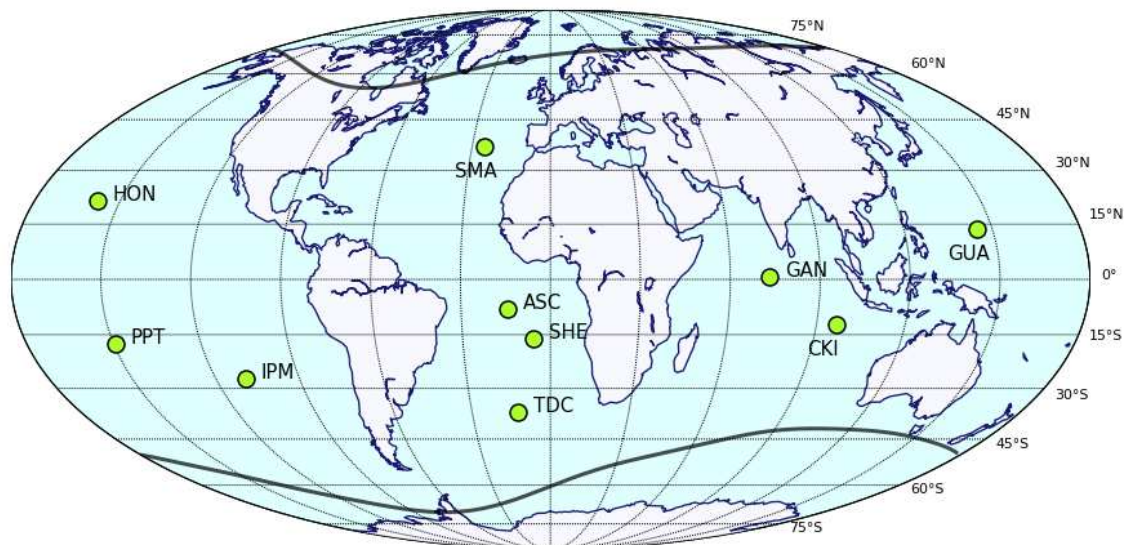


Figure 1. : Location of geomagnetic observatories used in this study (green dots). Black lines depict $\pm 55^\circ$ quasi dipole latitudes. Relevant information about these observatories is summarized in Table 1.

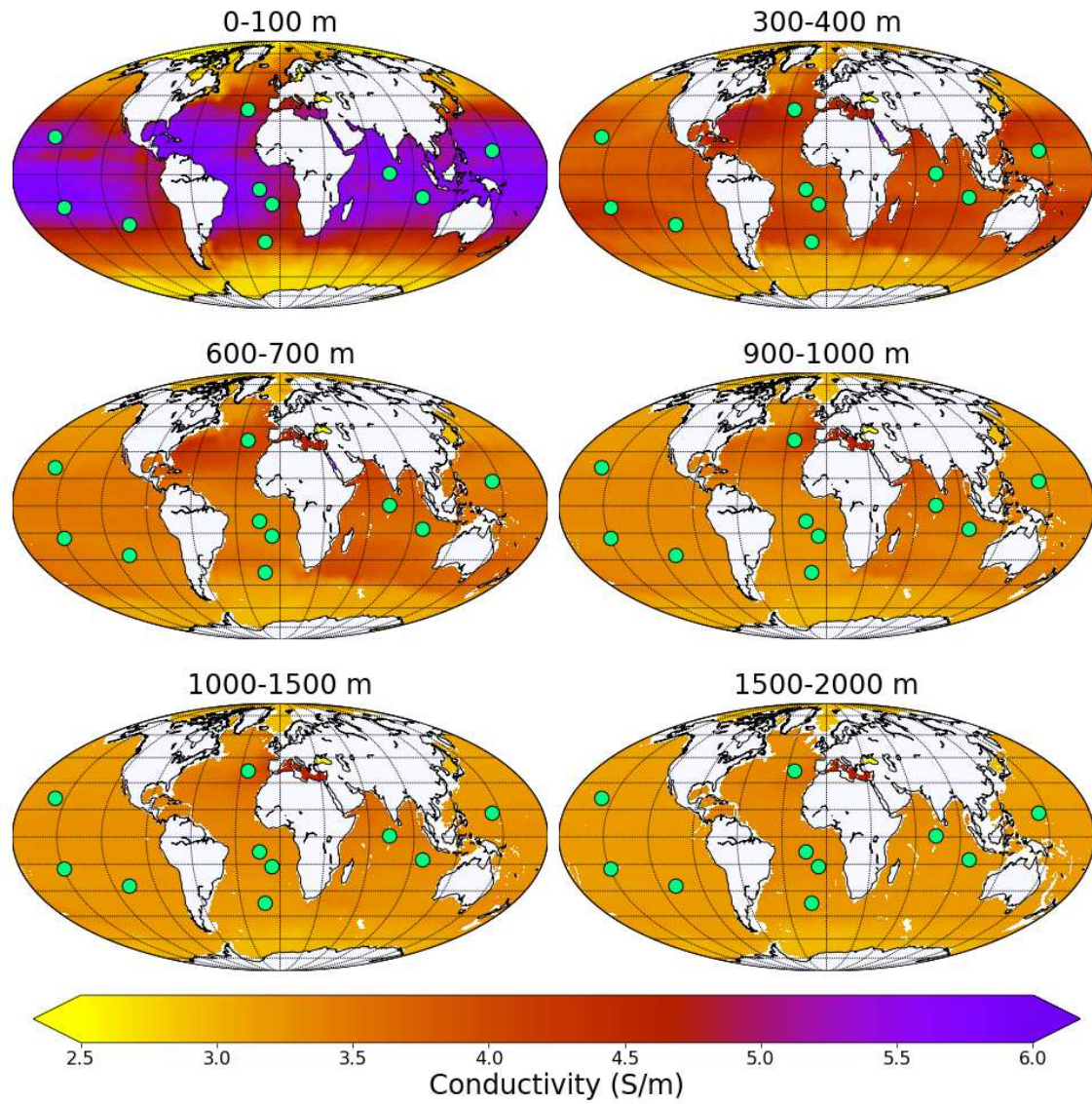


Figure 2. : Global maps of oceanic electric conductivity for six selected depth intervals for December 2015 model. Green dots denote the locations of the geomagnetic observatories used in this study.

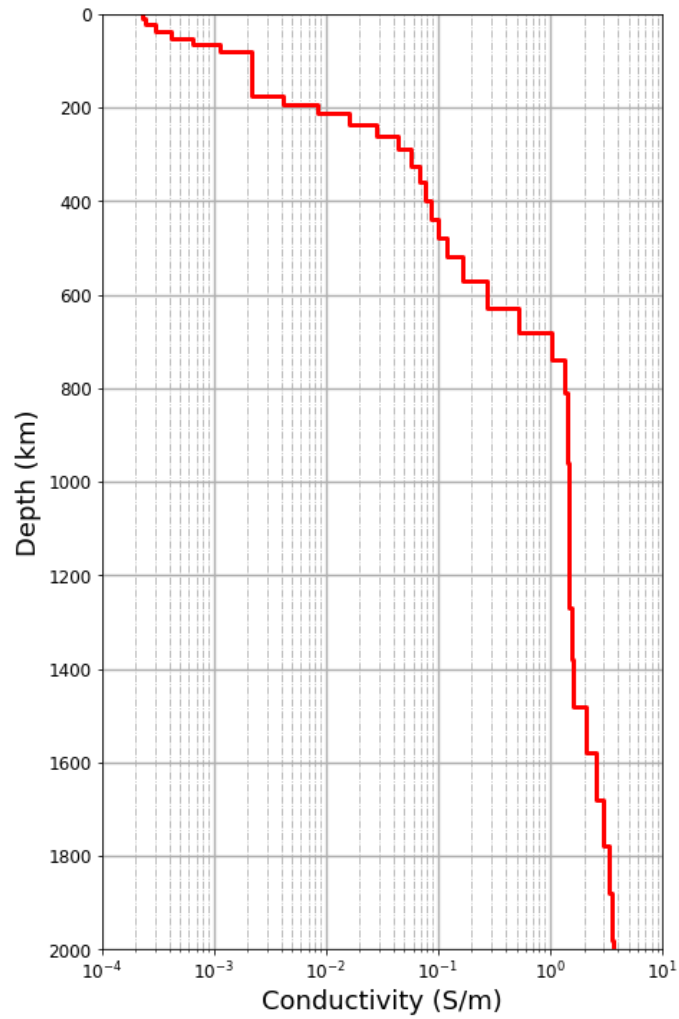


Figure 3. : 1-D global conductivity profile (from Grayver et al, 2017) used in this study for the crust and mantle beneath the 3-D (oceanic) modeling domain.

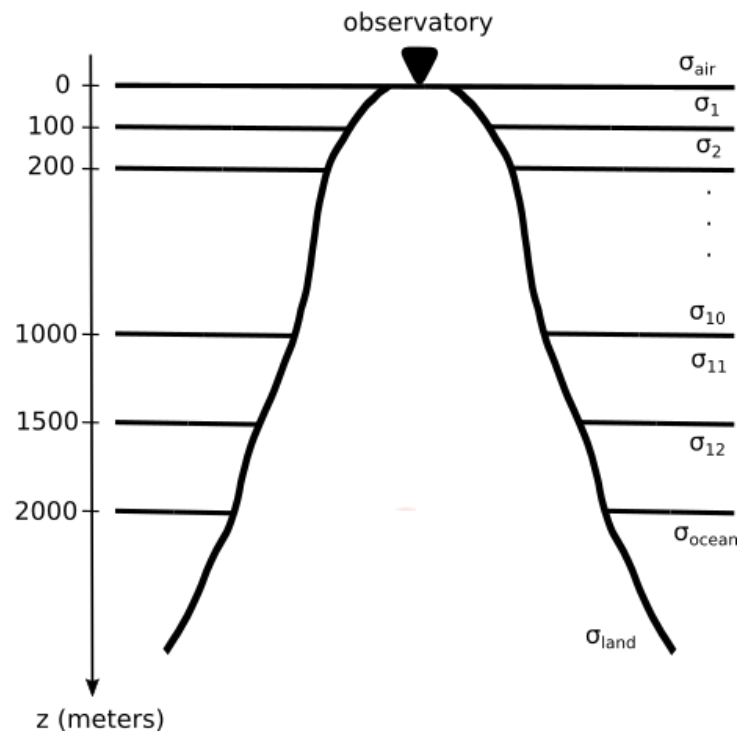


Figure 4. : Vertical parametrization of the conductivity distribution in the 3-D modelling domain. σ_1 to σ_{12} is the respective water layer's conductivity, set to the layers's average conductivity calculated from the global ocean conductivity model. σ_{ocean} is the deep (below 2000 m) ocean conductivity set to 3.2 S/m. σ_{land} is the landmass conductivity set to 0.01 S/m.

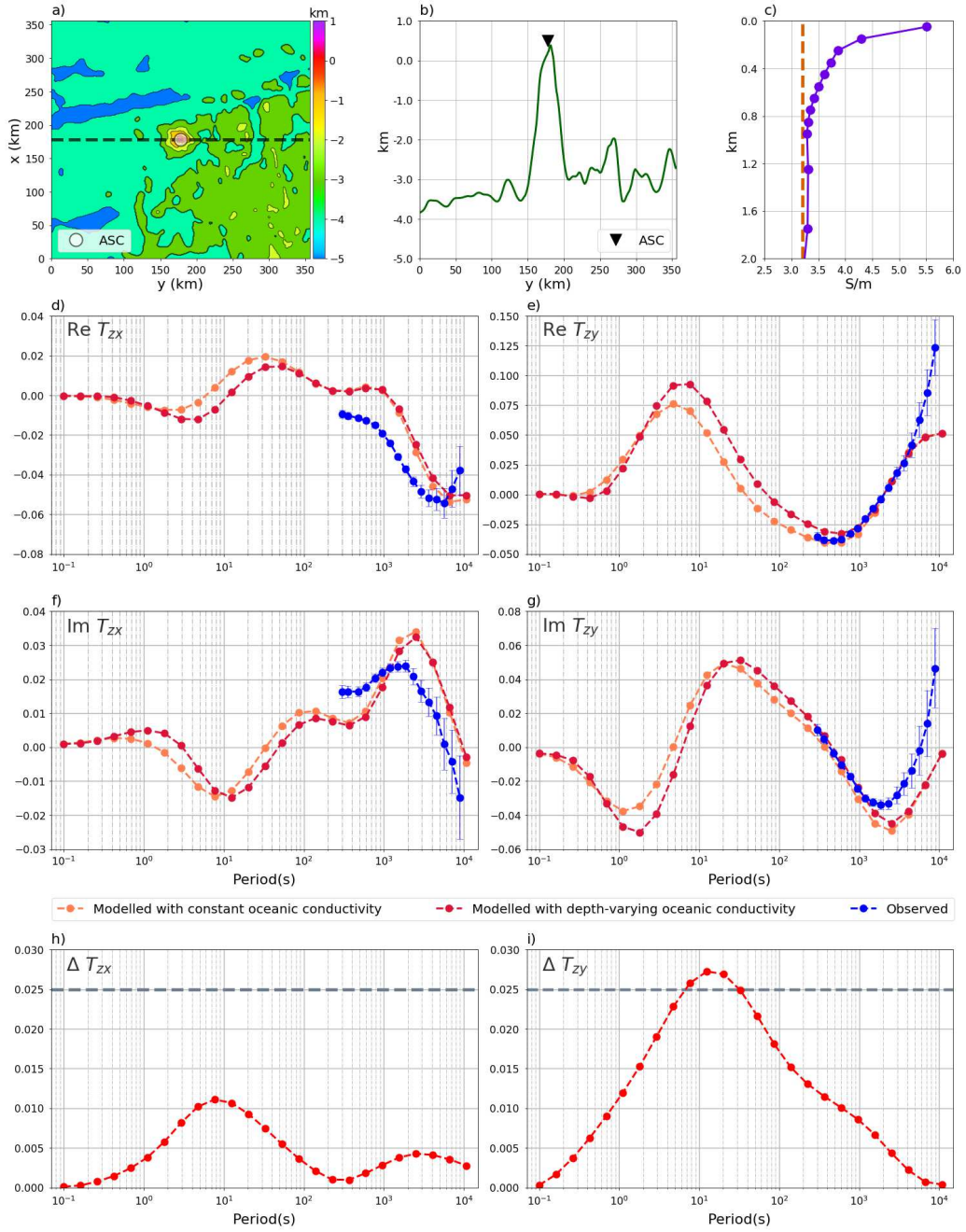


Figure 5. : Results for Ascension Island observatory (ASC). (a) Map of bathymetry; dashed line indicates location of profile shown in panel (b). (b) West-East oriented bathymetry profile. (c) Regional depth-varying (purple) oceanic conductivity and constant reference oceanic conductivity (3.2 S/m, red dashed line). (d) to (g) Real and imaginary parts for x and y components of tippers computed in the model with depth-varying (orange dots and dashed line) and depth-constant (red dots and dashed line) oceanic conductivity. (h) Difference for the computed tipper x component between depth-varying and depth-constant ocean conductivity, see text for details. Dashed grey line indicates the threshold of 0.025. (i) Same as (h), but for the y component.

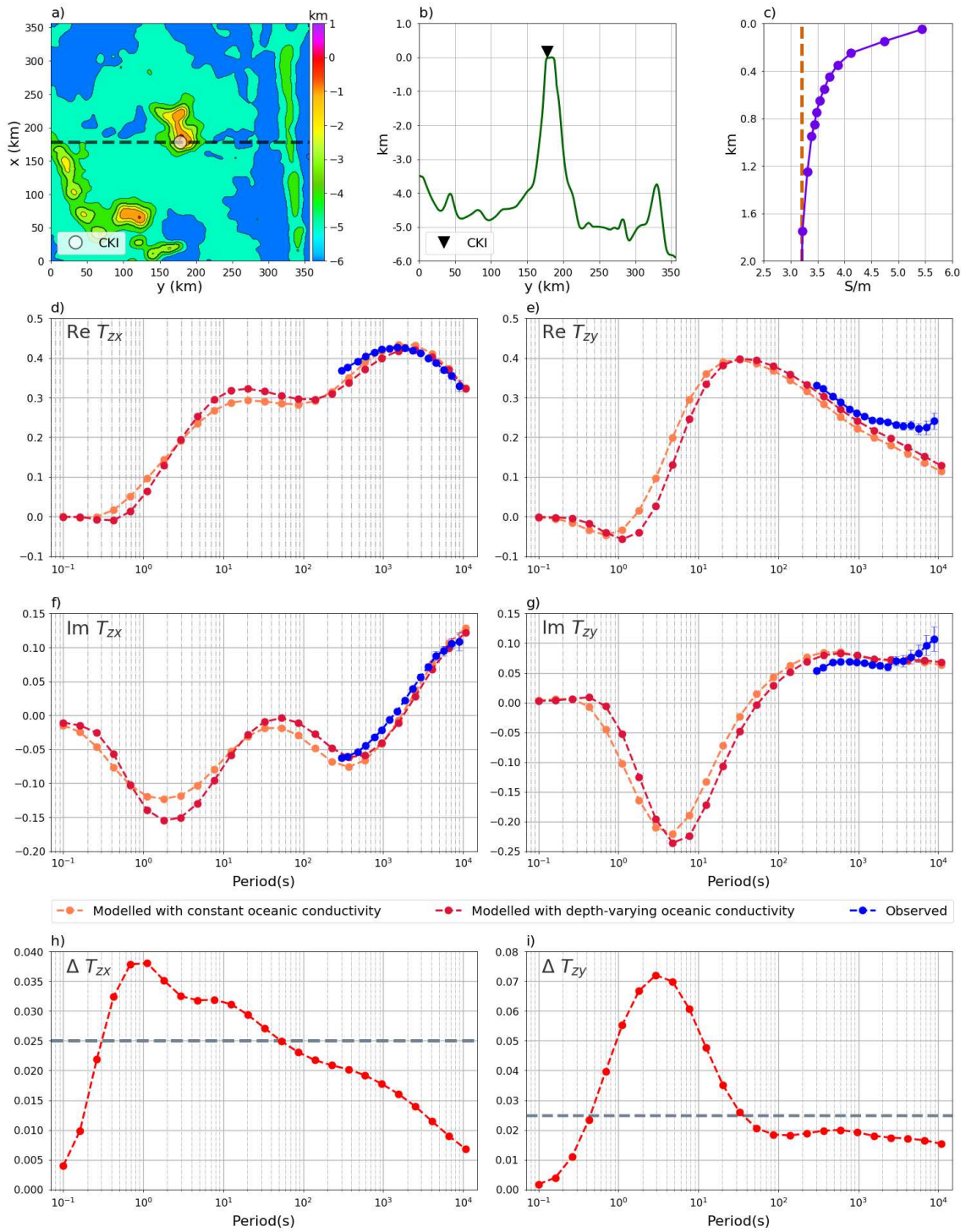


Figure 6. : Same as Figure 5, but for Cocos-Keeling Islands observatory (CKI).

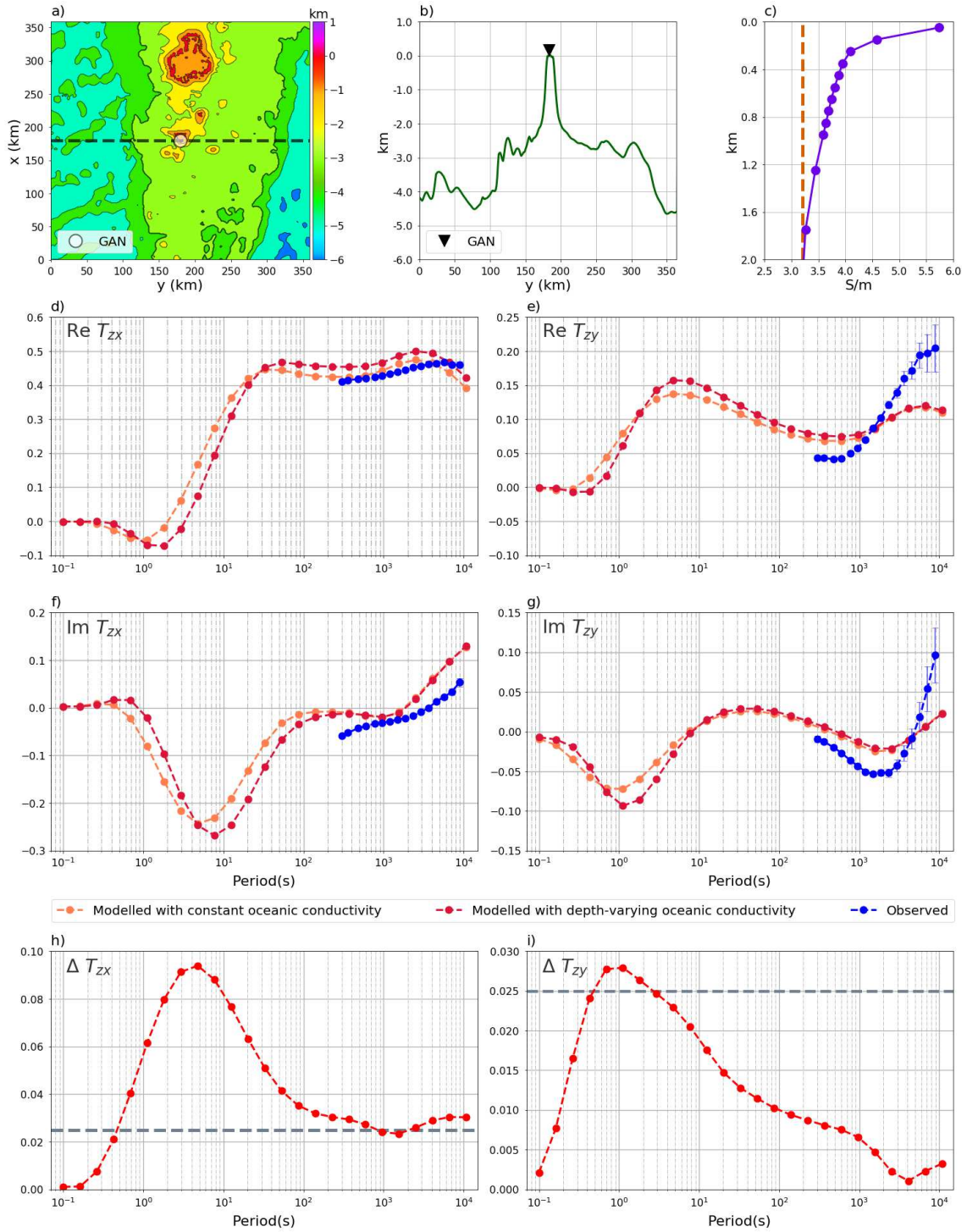


Figure 7. : Same as Figure 5, but for Gan observatory (GAN).

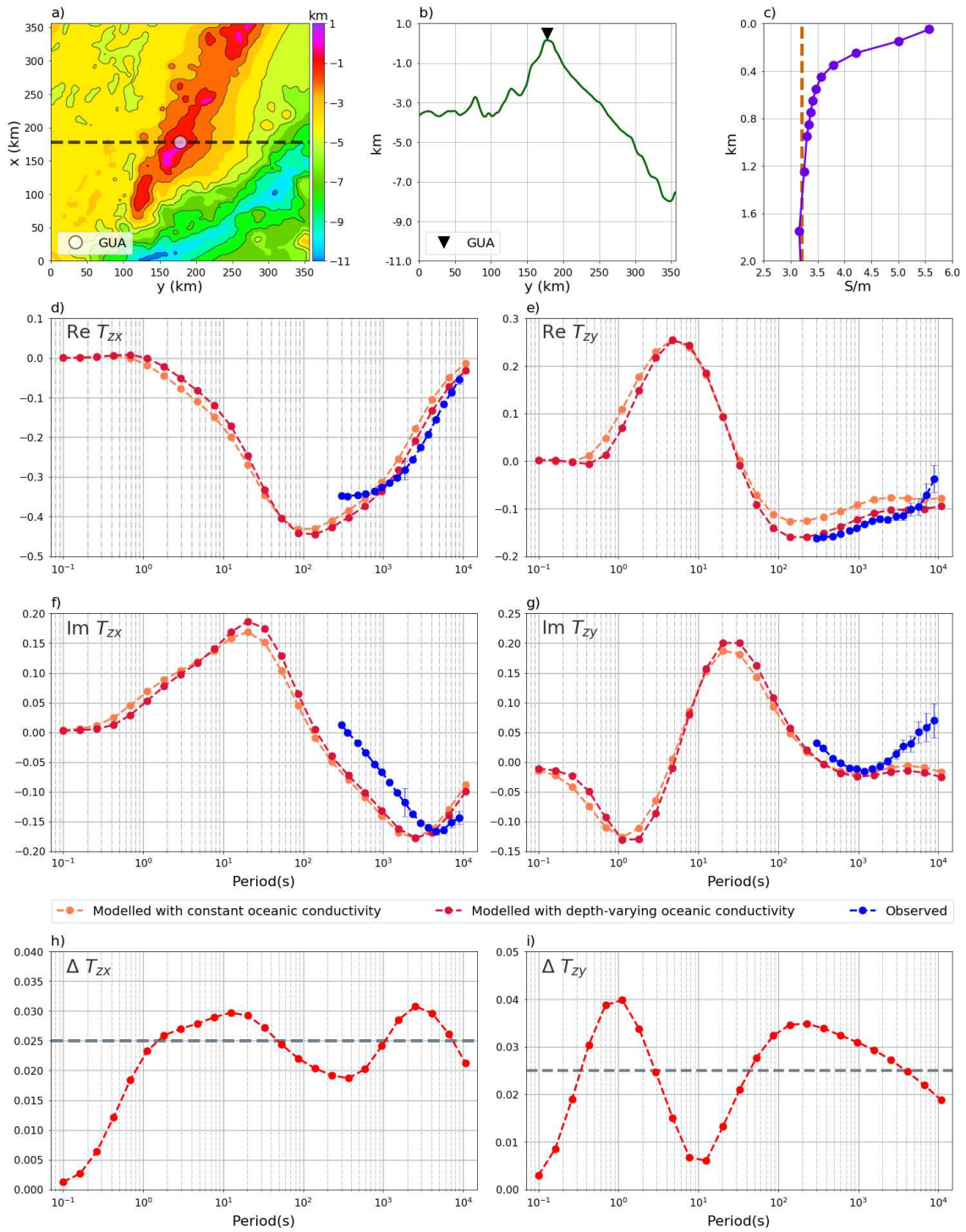


Figure 8. : Same as Figure 5, but for Guam observatory (GUA).

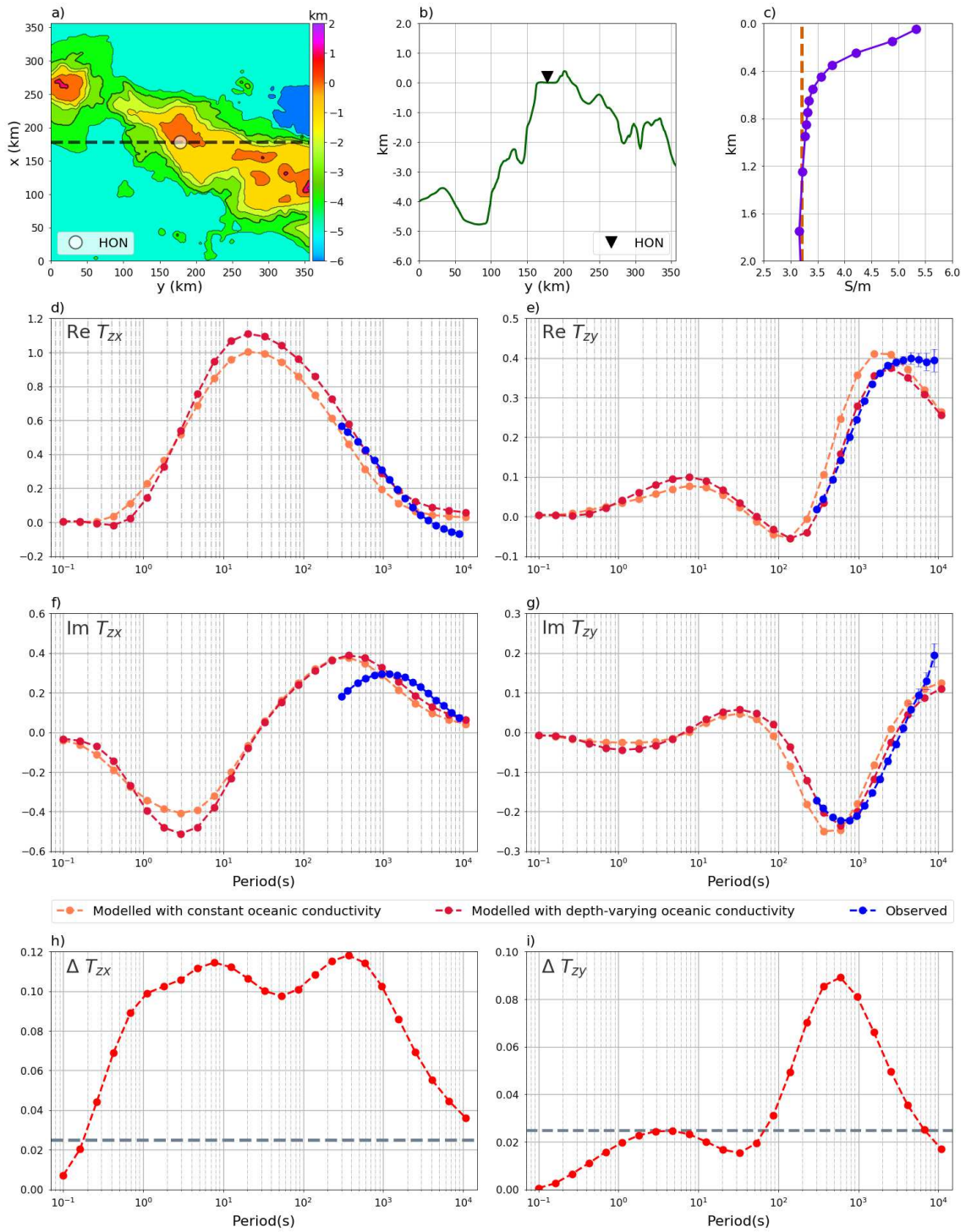


Figure 9. : Same as Figure 5, but for Honolulu observatory (HON).

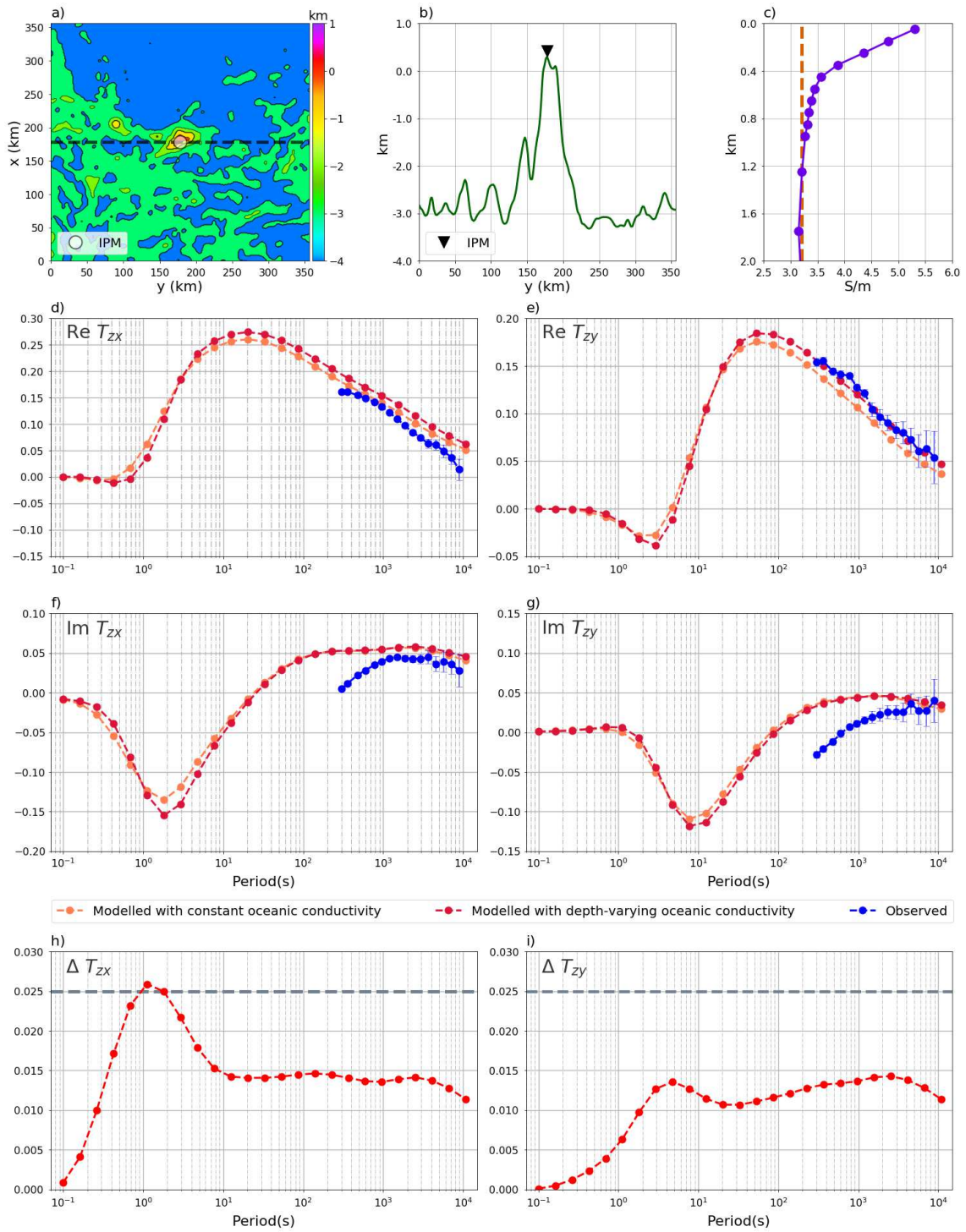


Figure 10. : Same as Figure 5, but for Easter Island observatory (IPM).

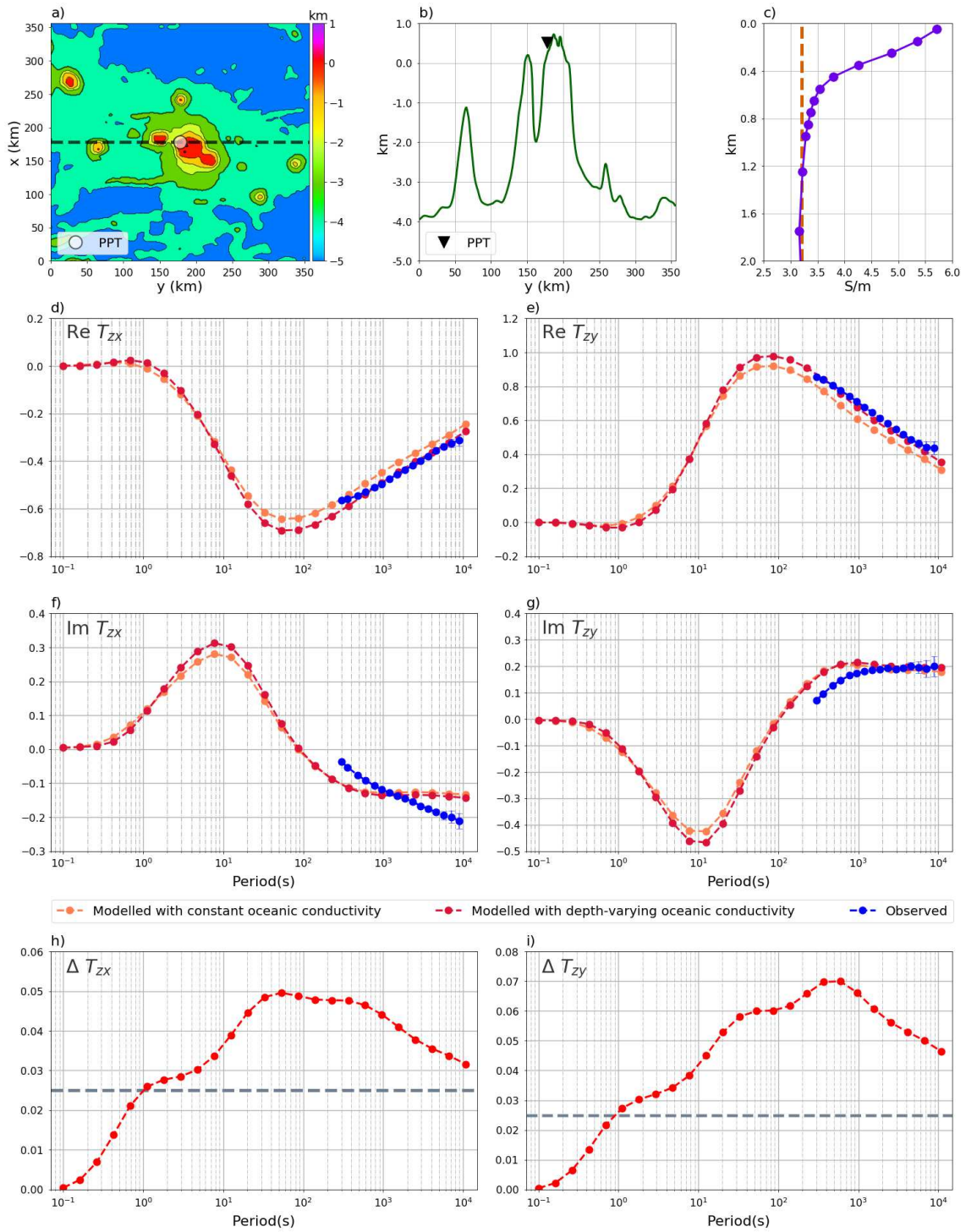


Figure 11. : Same as Figure 5, but for Pamatai observatory (PPT).

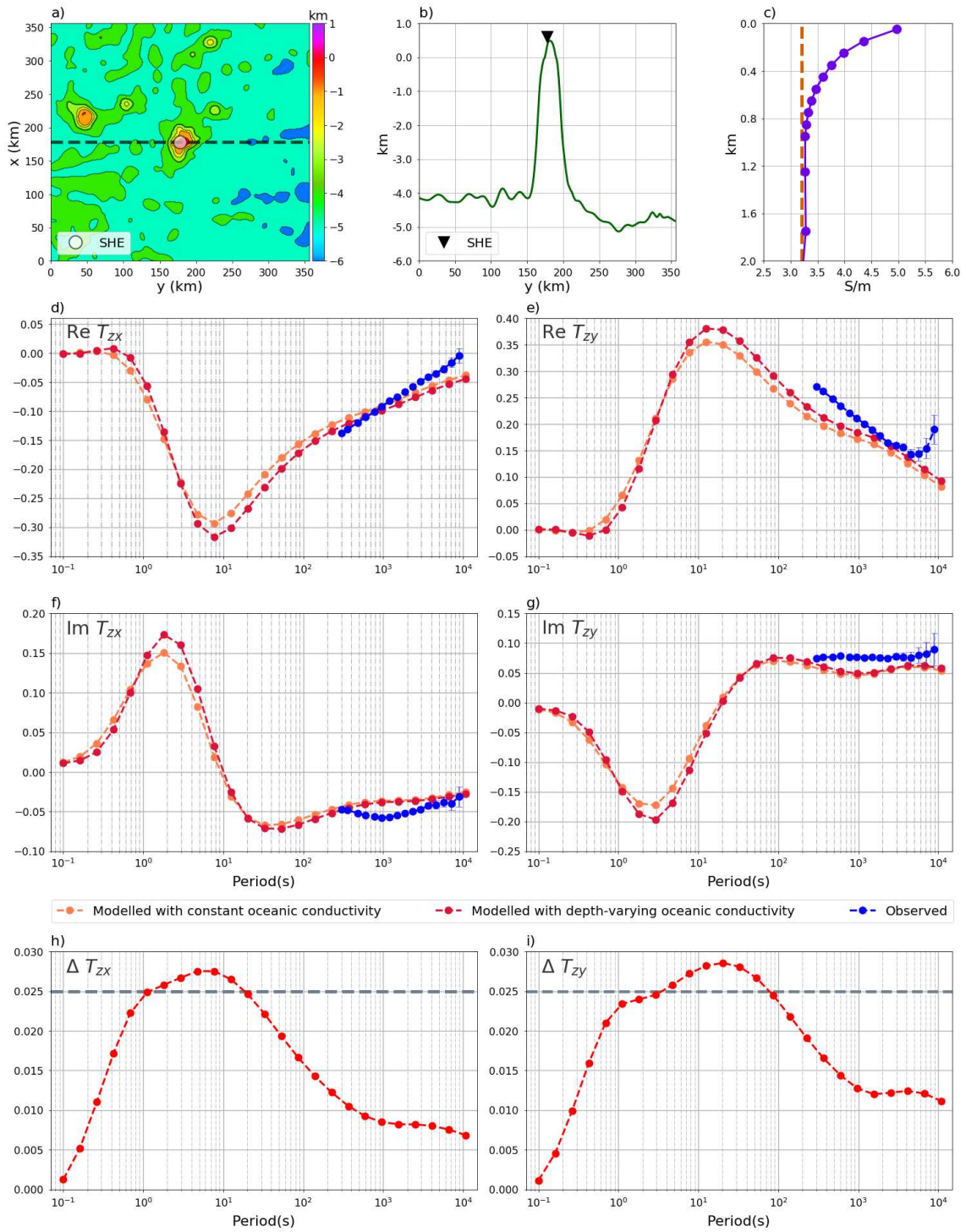


Figure 12. : Same as Figure 5, but for St. Helena observatory (SHE).

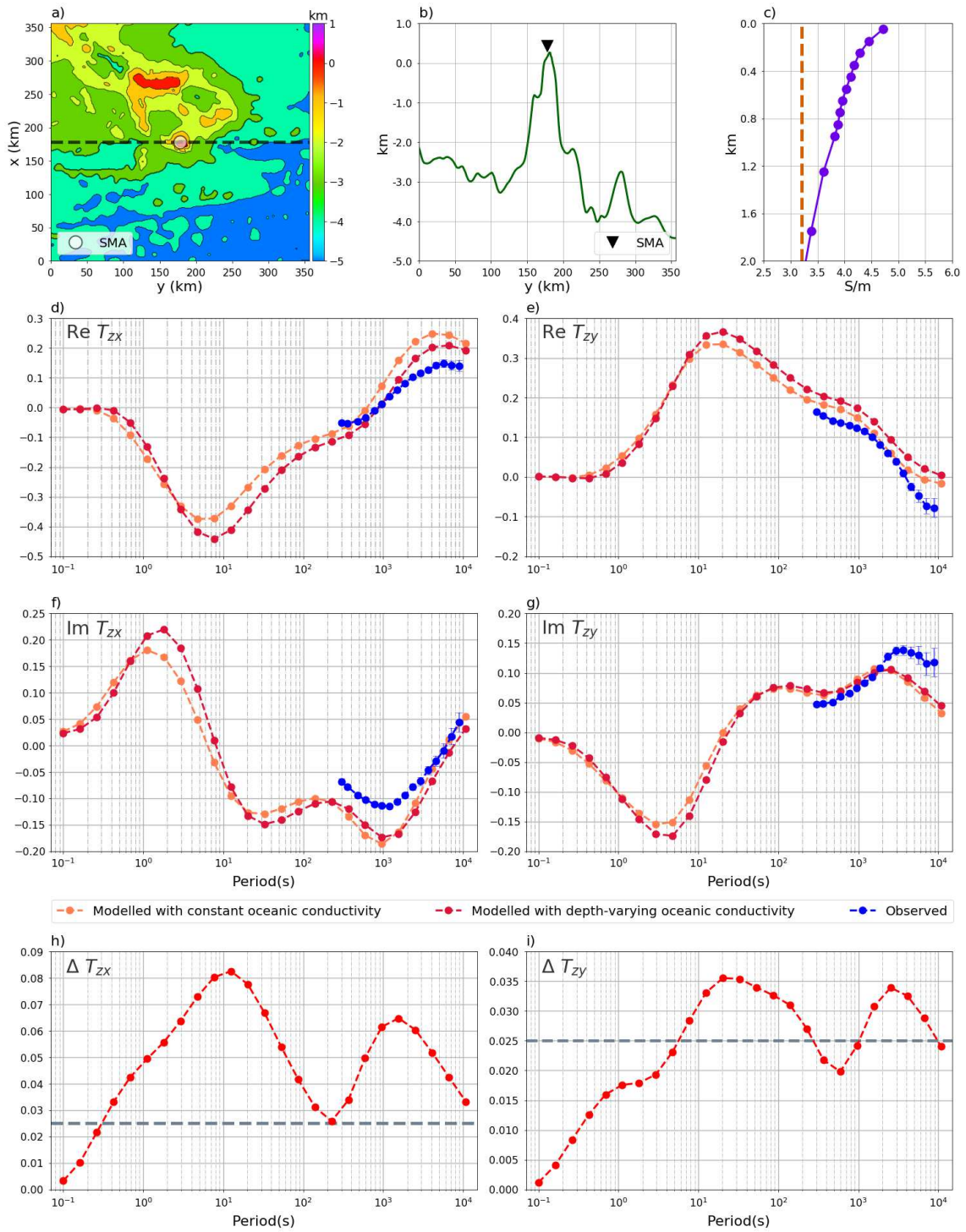


Figure 13. : Same as Figure 5, but for Santa-Maria/Azores observatory (SMA).

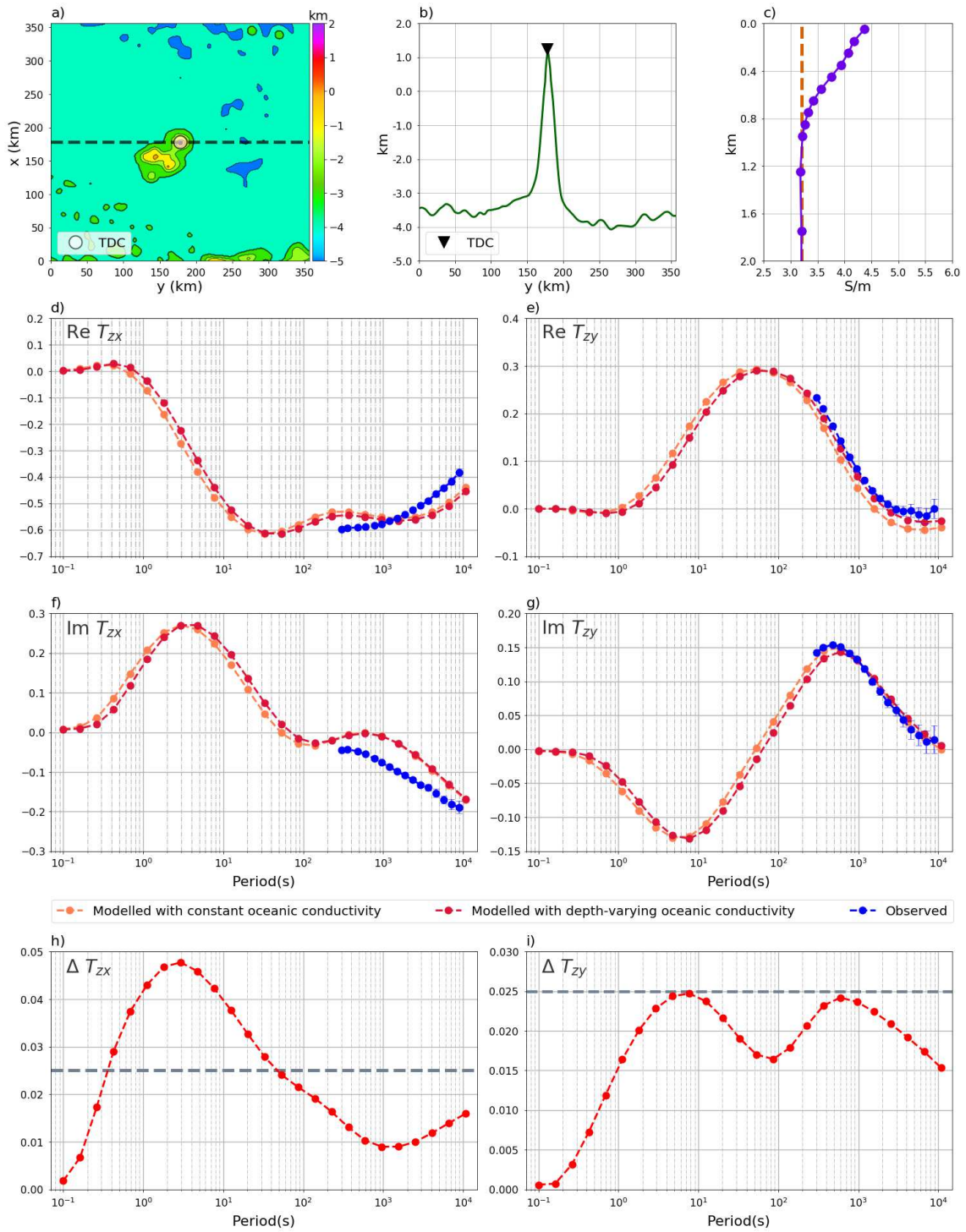


Figure 14. : Same as Figure 5, but for Tristan da Cunha observatory (TDC).

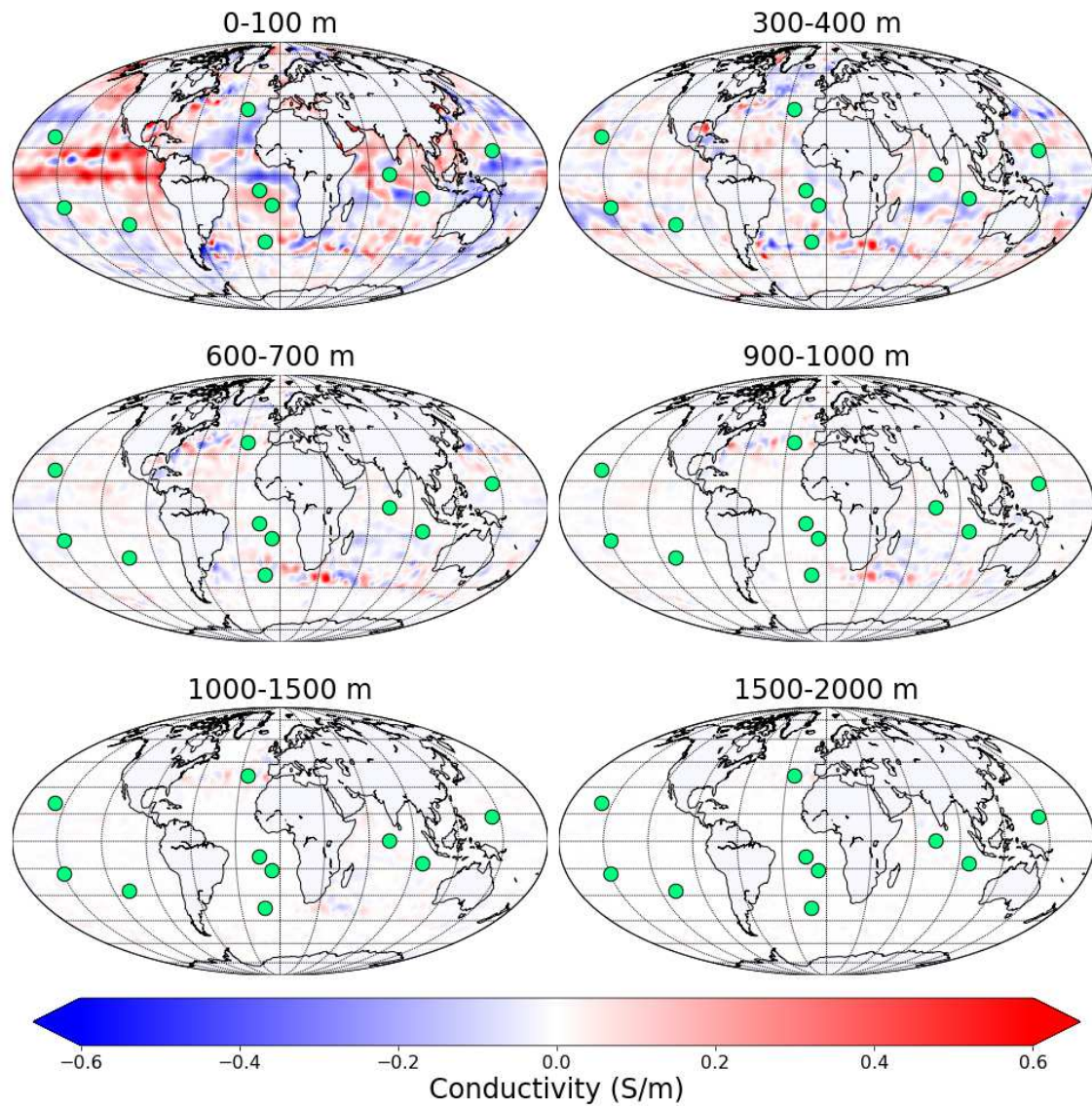


Figure 15. : Global maps of difference between 2015 December and June oceanic conductivity models at six depth intervals. Green circles denote locations of geomagnetic observatories used in this study.

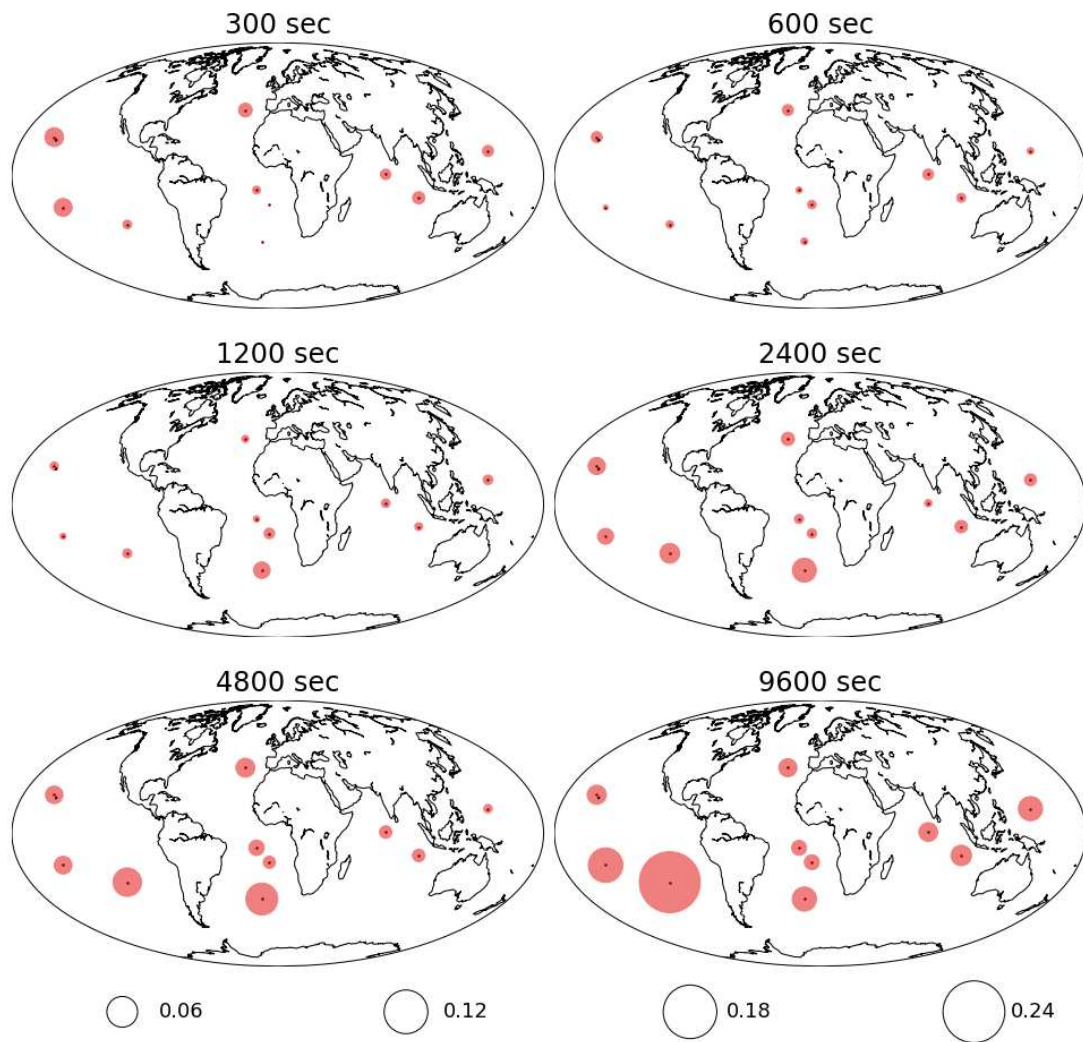


Figure 16. : Difference between “December” and “June” T_{zx} at island observatories, shown as filled circles. “Experimental” and “modeled” differences are colored by light and dark red, respectively. The size of circles below the plots indicates four ranges of differences.

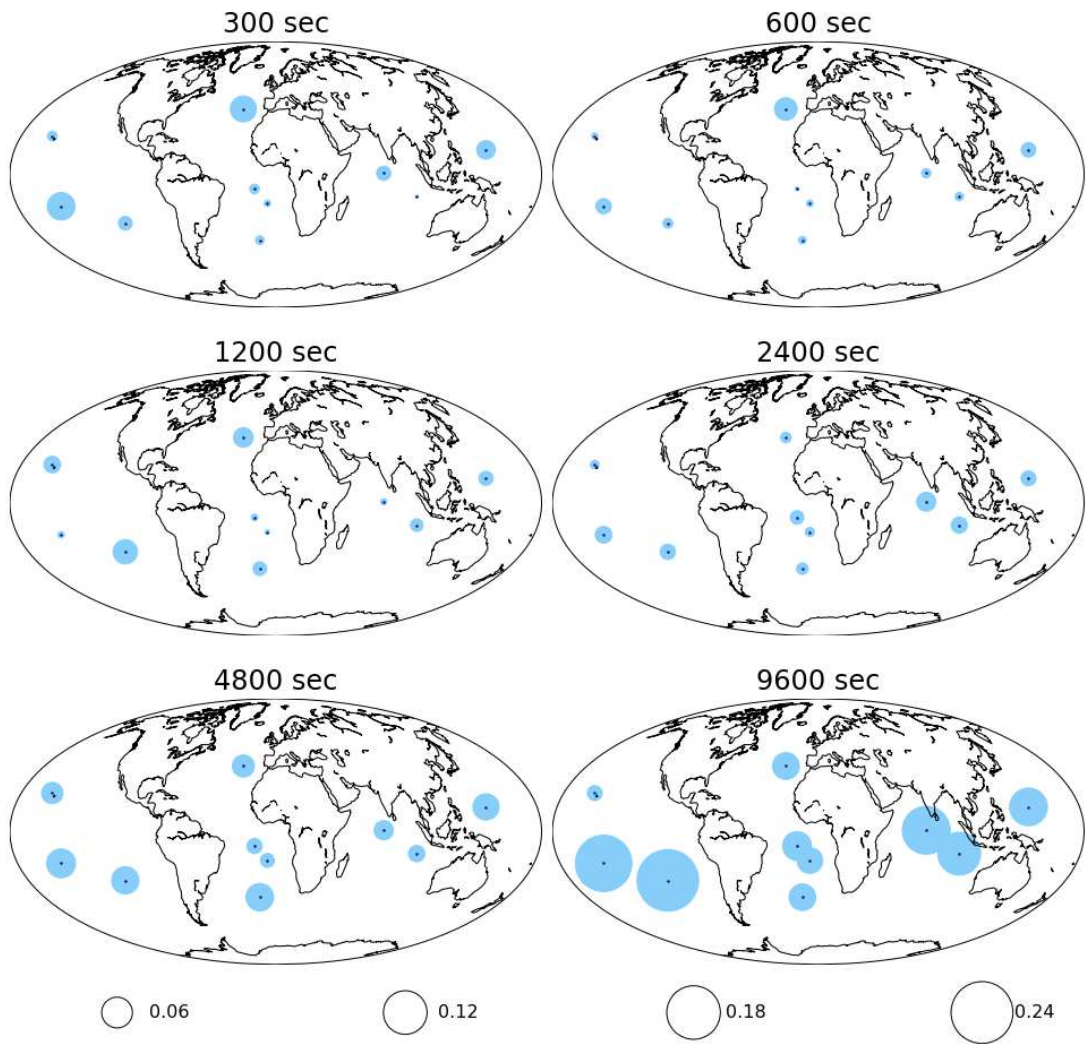


Figure 17. : Same as Figure 16, but for T_{zy} .

Figures

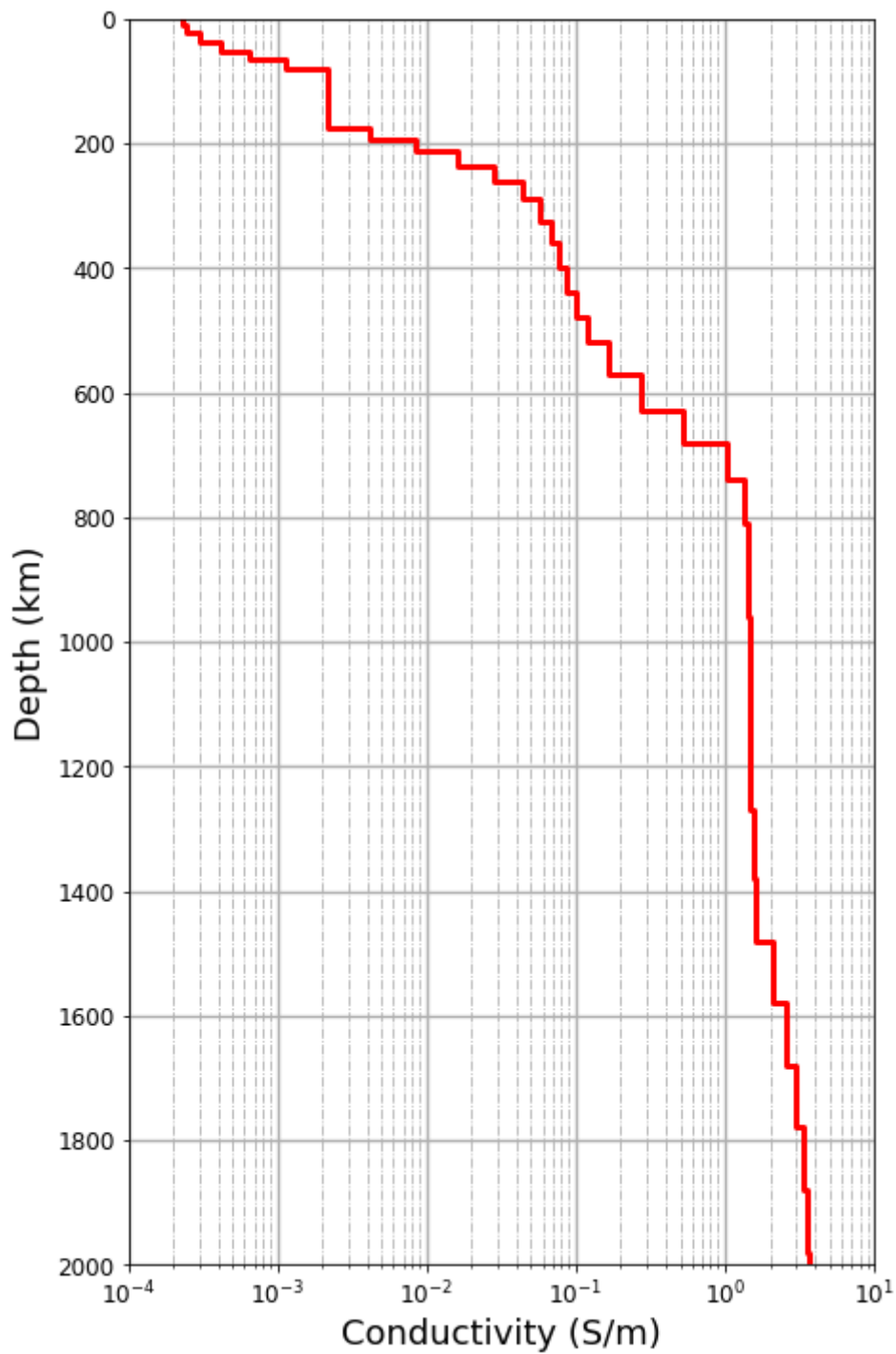


Figure 1

Location of geomagnetic observatories used in this study (green dots). Black lines depict $\pm 55^\circ$ quasi dipole latitudes. Relevant information about these observatories is summarized in Table 1.

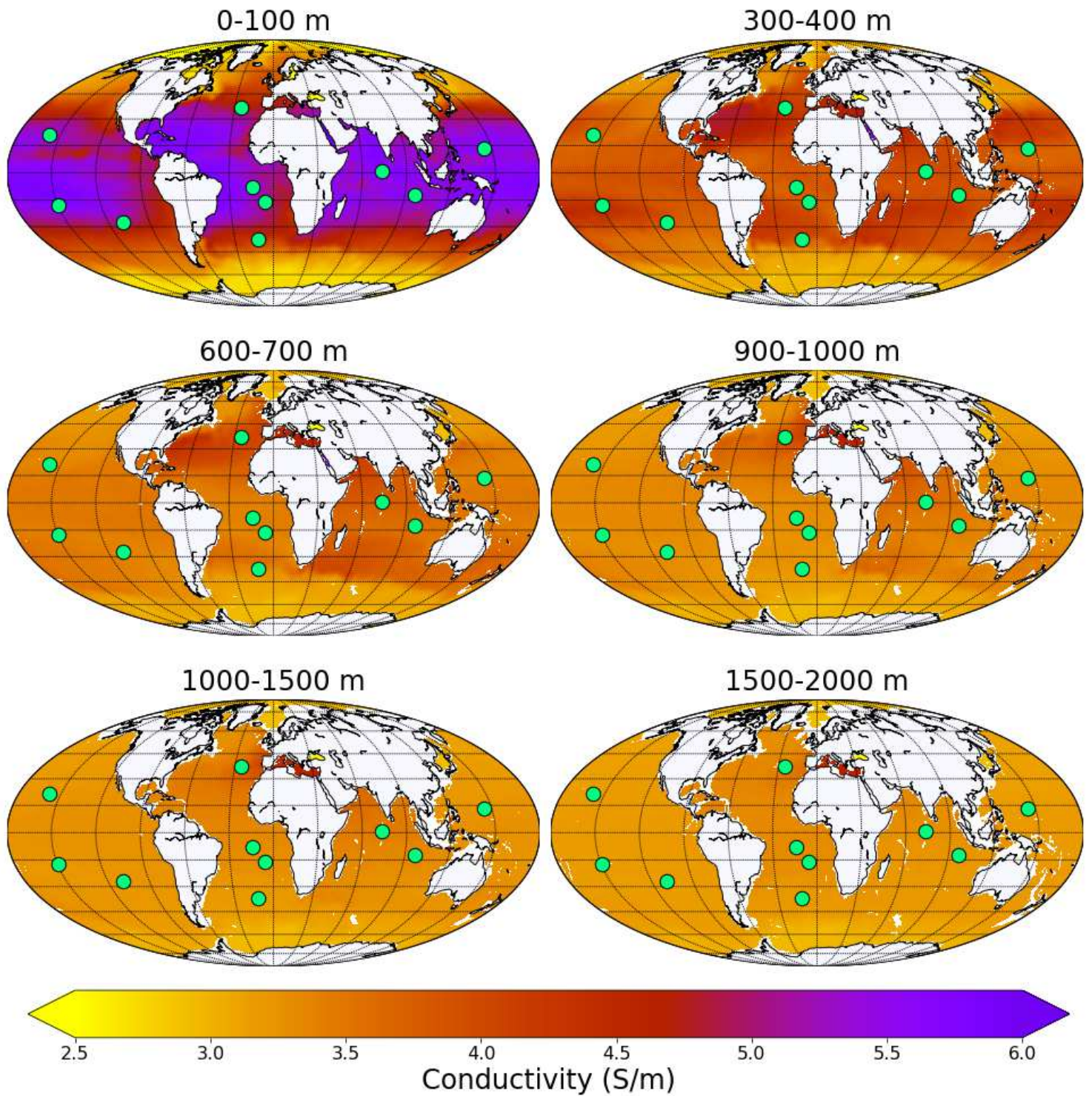


Figure 2

Global maps of oceanic electric conductivity for six selected depth intervals for December 2015 model. Green dots denote the locations of the geomagnetic observatories used in this study

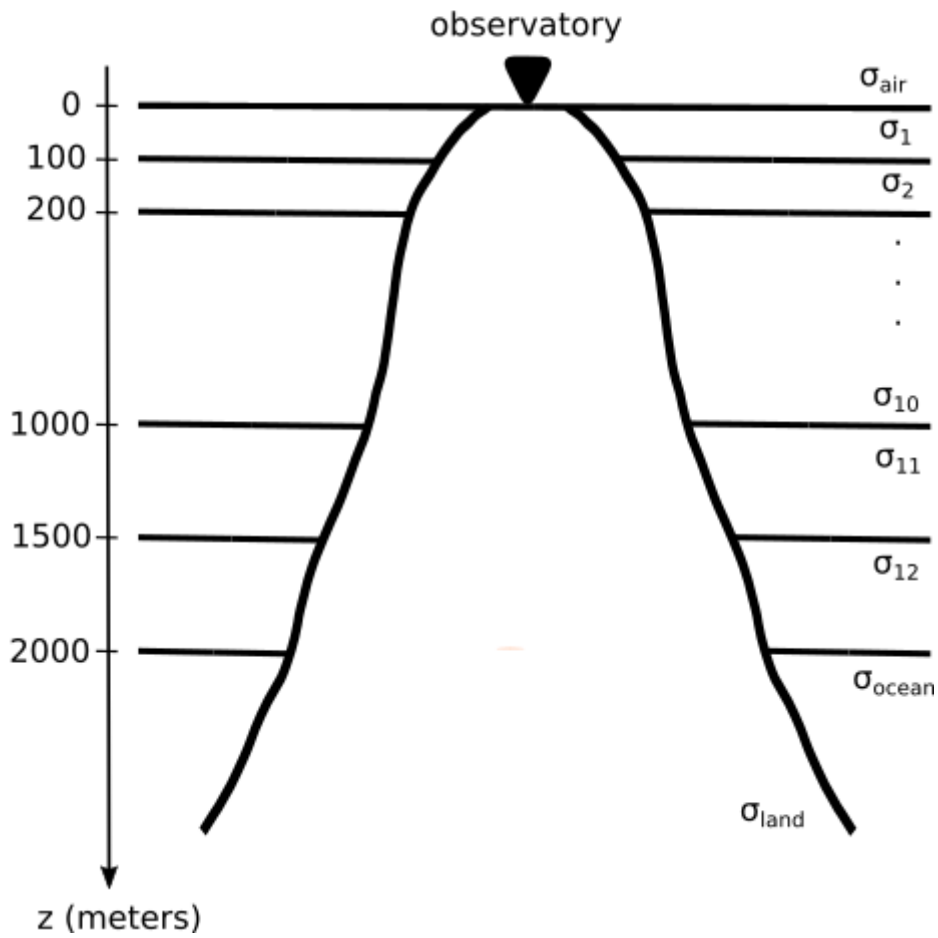


Figure 3

1-D global conductivity profile (from Grayver et al, 2017) used in this study for the crust and mantle beneath the 3-D (oceanic) modeling domain

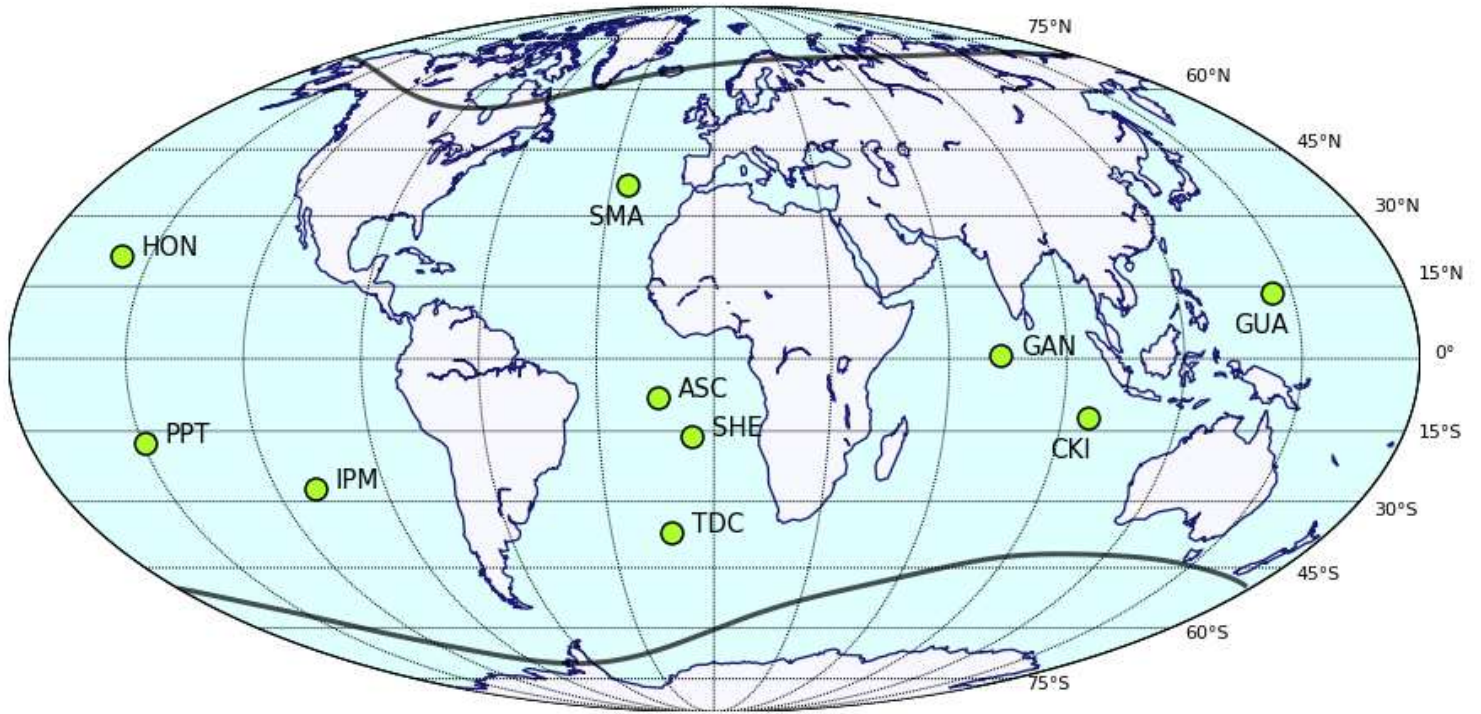


Figure 4

Vertical parametrization of the conductivity distribution in the 3-D modelling domain. σ_1 to σ_{12} is the respective water layer's conductivity, set to the layers's average conductivity calculated from the global ocean conductivity model. σ_{ocean} is the deep (below 2000 m) ocean conductivity set to 3.2 S/m. σ_{land} is the landmass conductivity set to 0.01 S/m.

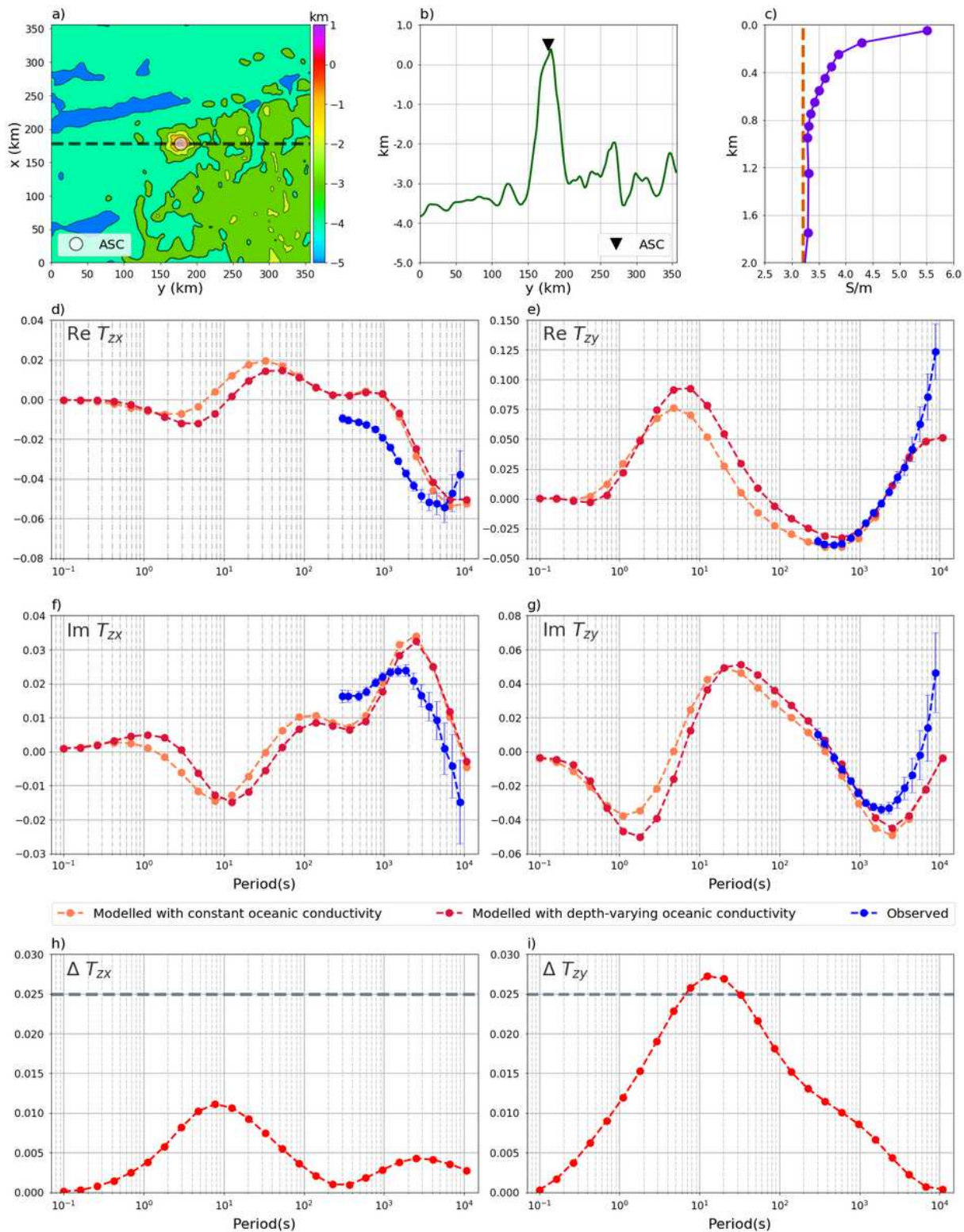


Figure 5

Results for Ascension Island observatory (ASC). (a) Map of bathymetry; dashed line indicates location of profile shown in panel (b). (b) West-East oriented bathymetry profile. (c) Regional depth-varying (purple) oceanic conductivity and constant reference oceanic conductivity (3.2 S/m, red dashed line). (d) to (g) Real and imaginary parts for x and y components of tippers computed in the model with depth-varying (orange dots and dashed line) and depth-constant (red dots and dashed line) oceanic conductivity. (h)

Difference for the computed tipper x component between depth-varying and depth-constant ocean conductivity, see text for details. Dashed grey line indicates the threshold of 0.025. (i) Same as (h), but for the y component.

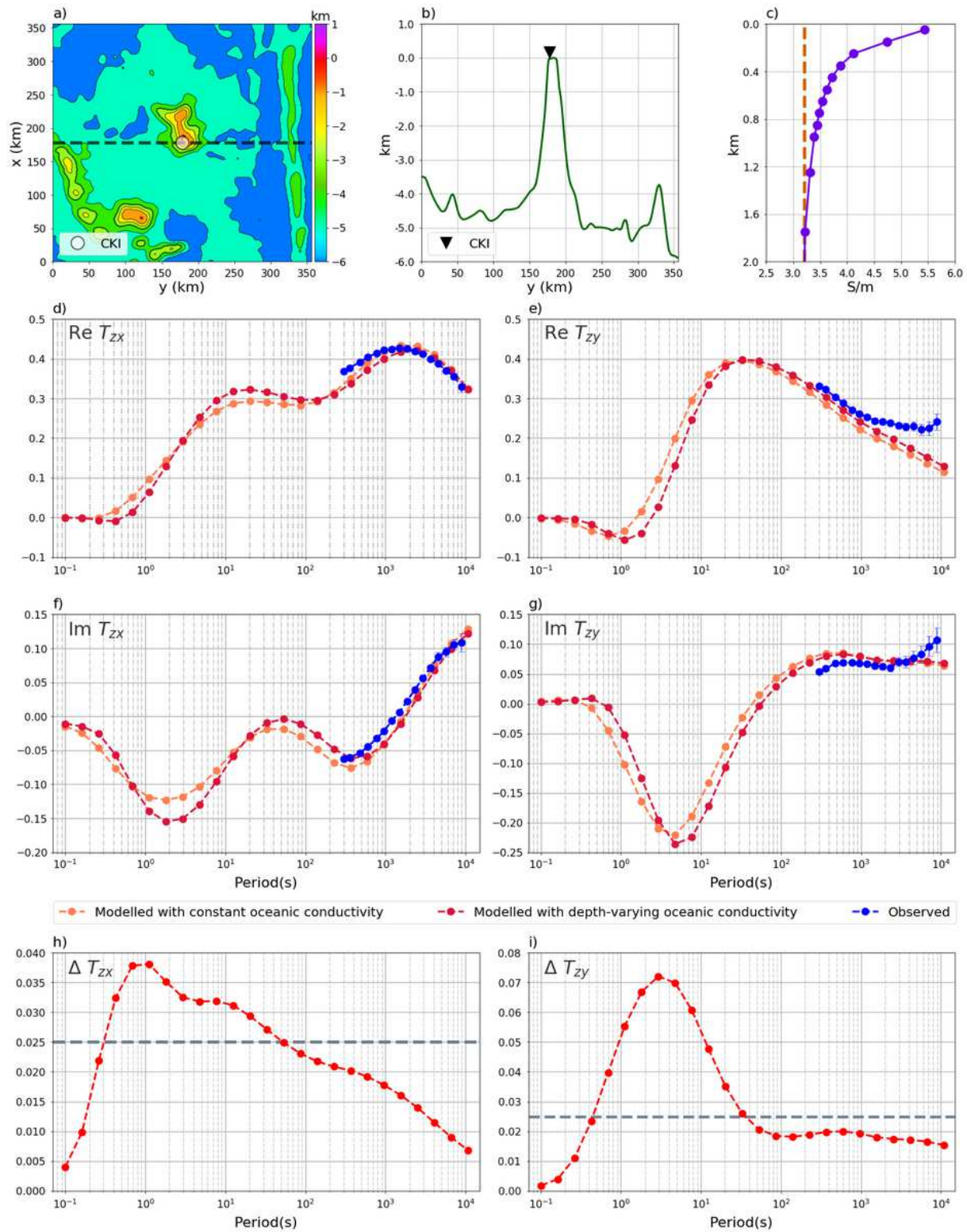


Figure 6

Same as Figure 5, but for Cocos-Keeling Islands observatory (CKI).

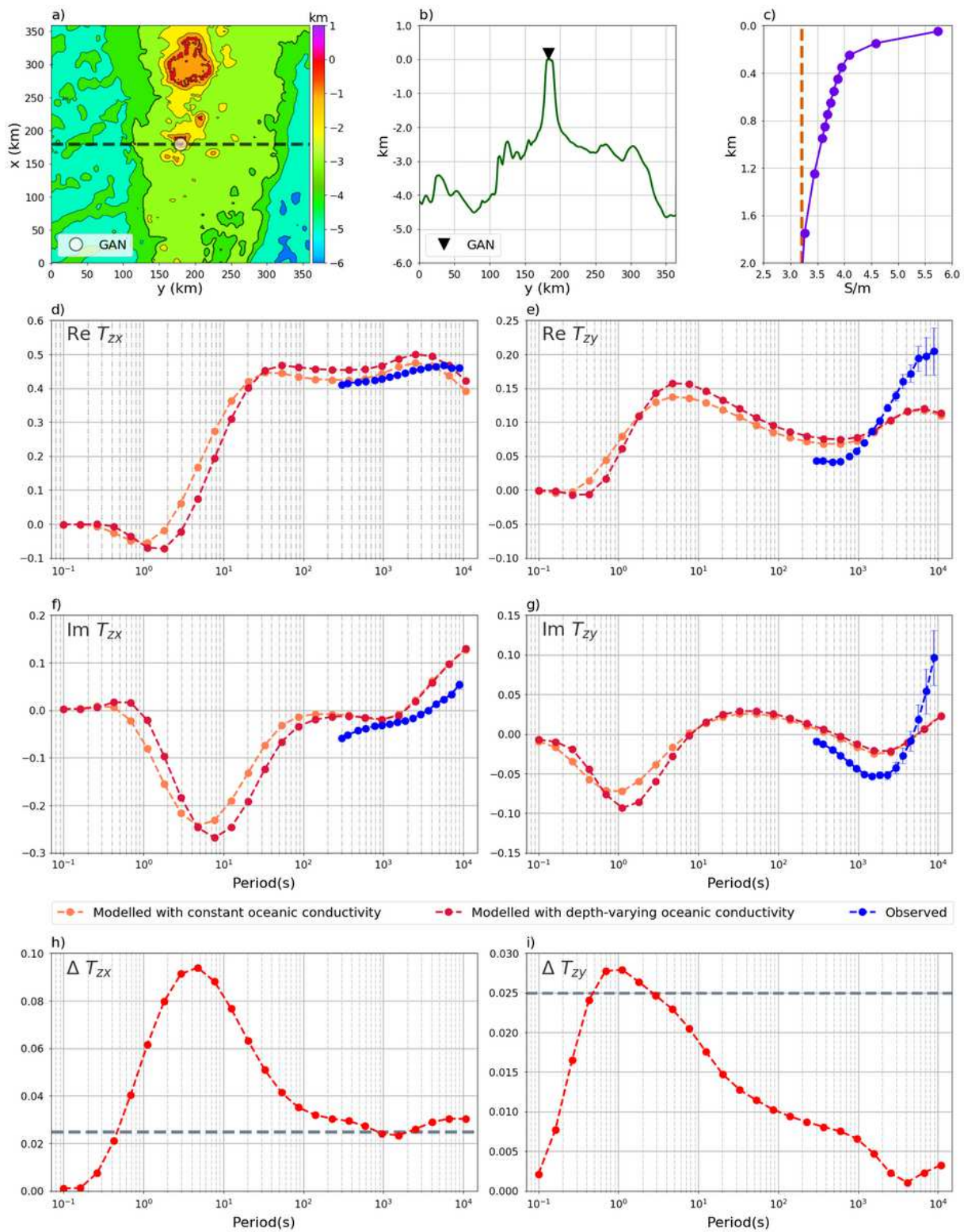


Figure 7

Same as Figure 5, but for Gan observatory (GAN).

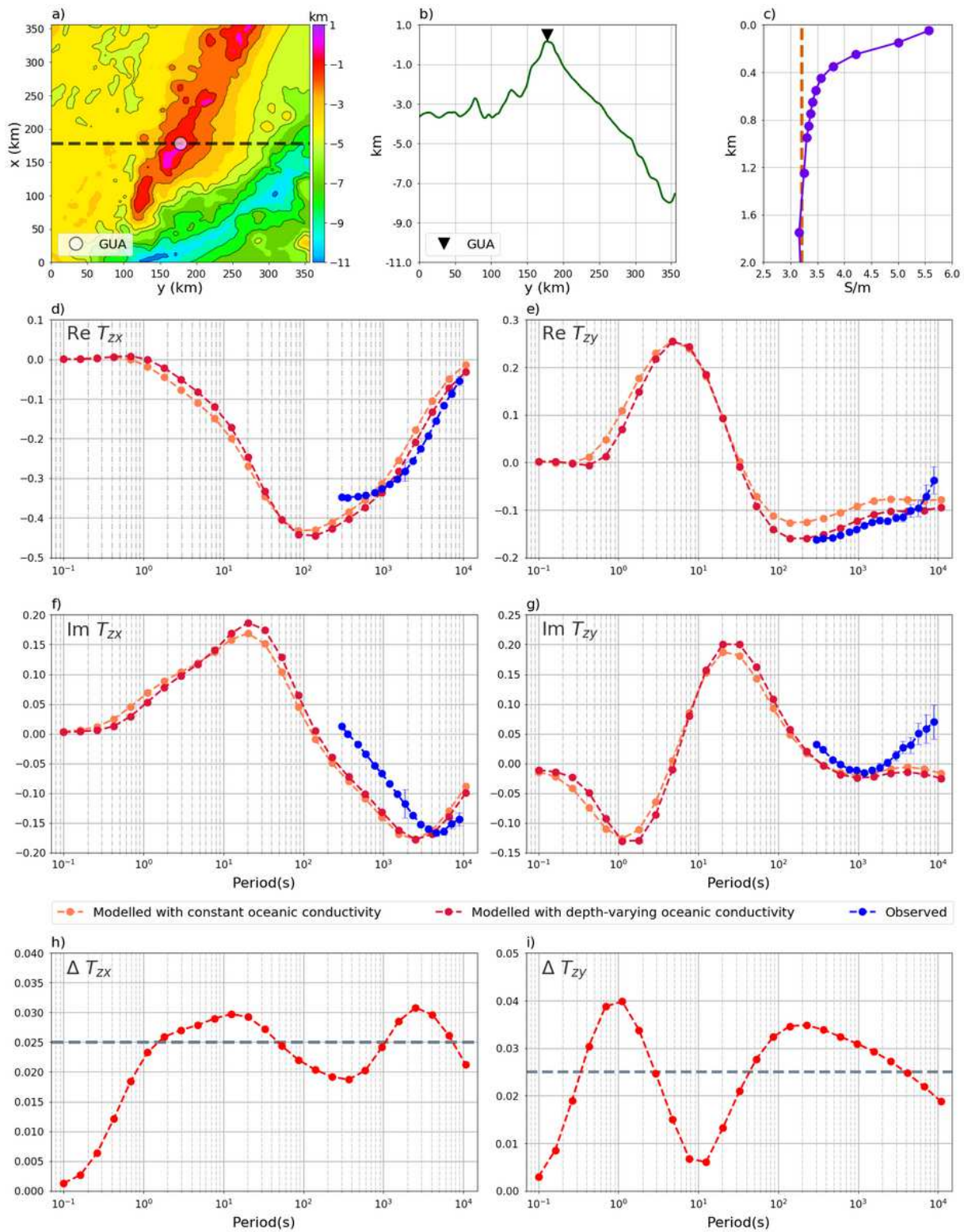


Figure 8

Same as Figure 5, but for Guam observatory (GUA).

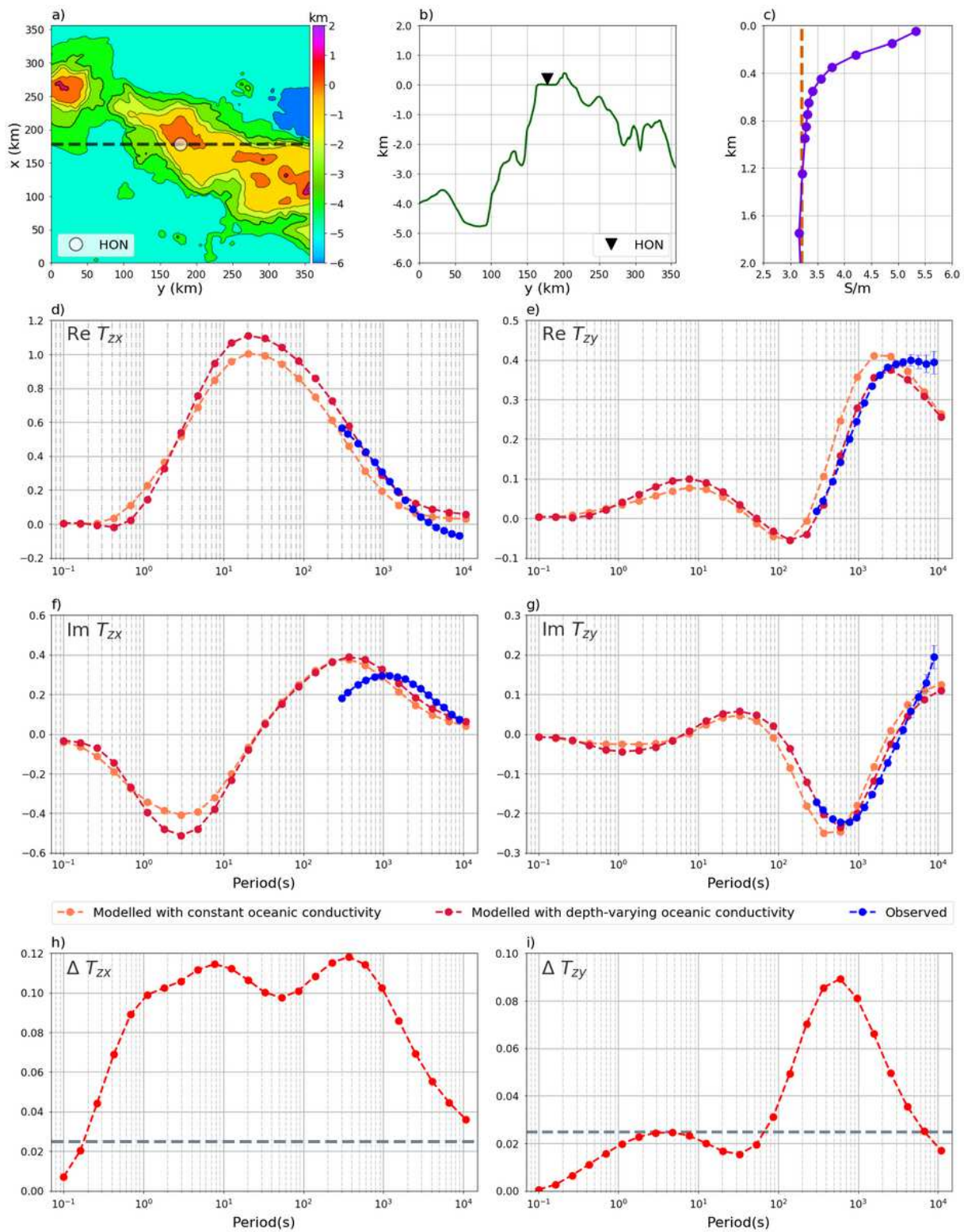


Figure 9

Same as Figure 5, but for Honolulu observatory (HON).

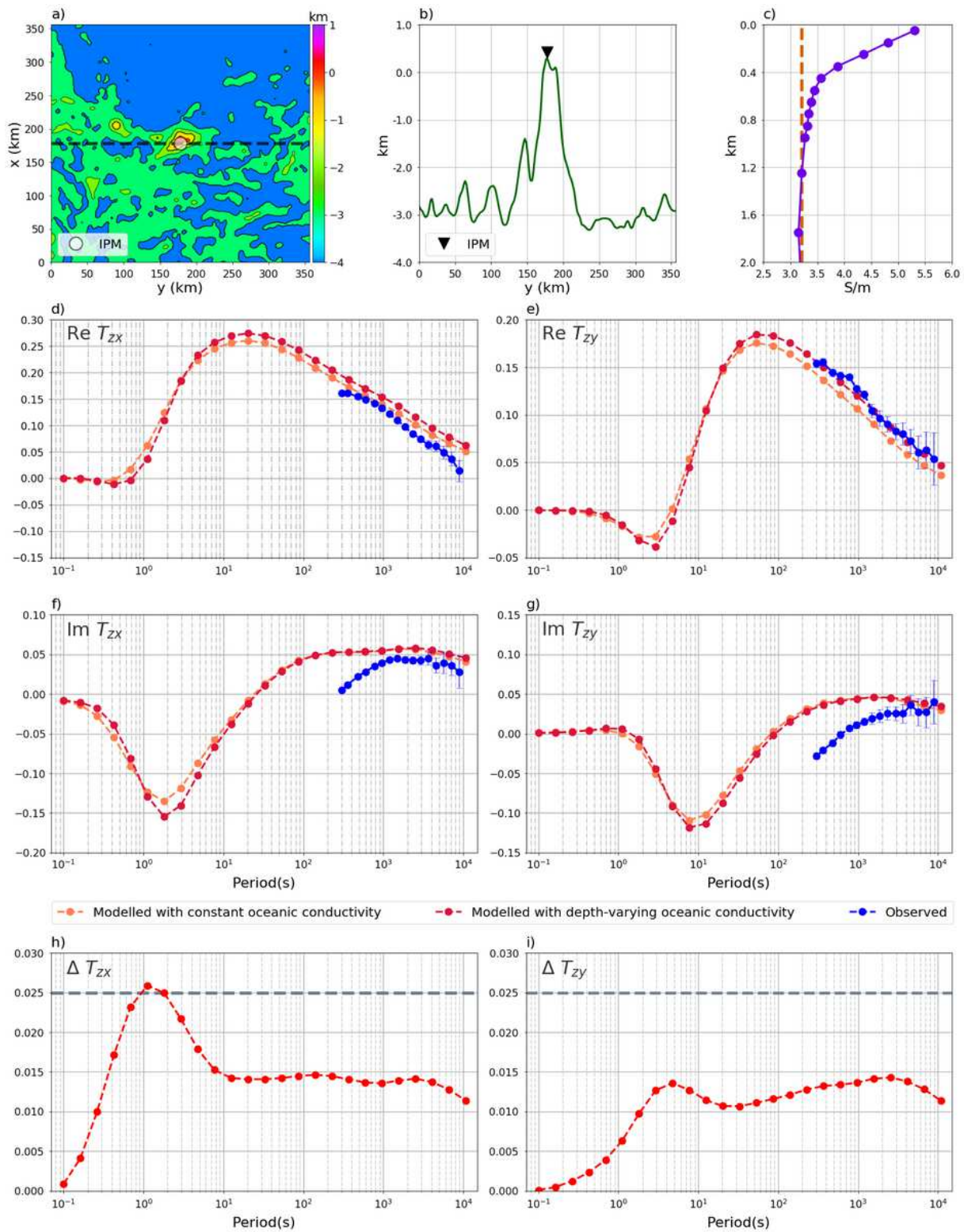


Figure 10

Same as Figure 5, but for Easter Island observatory (IPM).

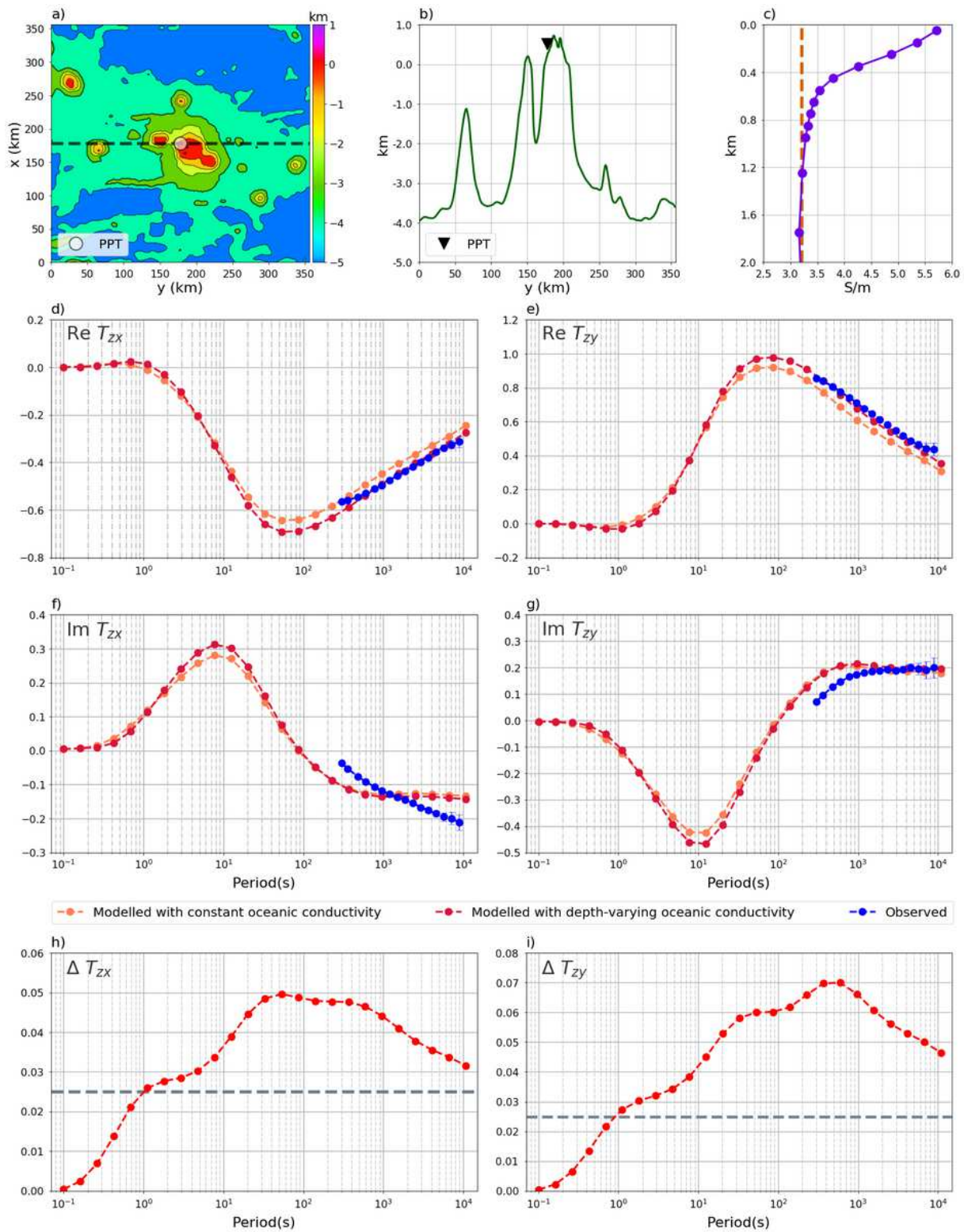


Figure 11

Same as Figure 5, but for Pamatai observatory (PPT).

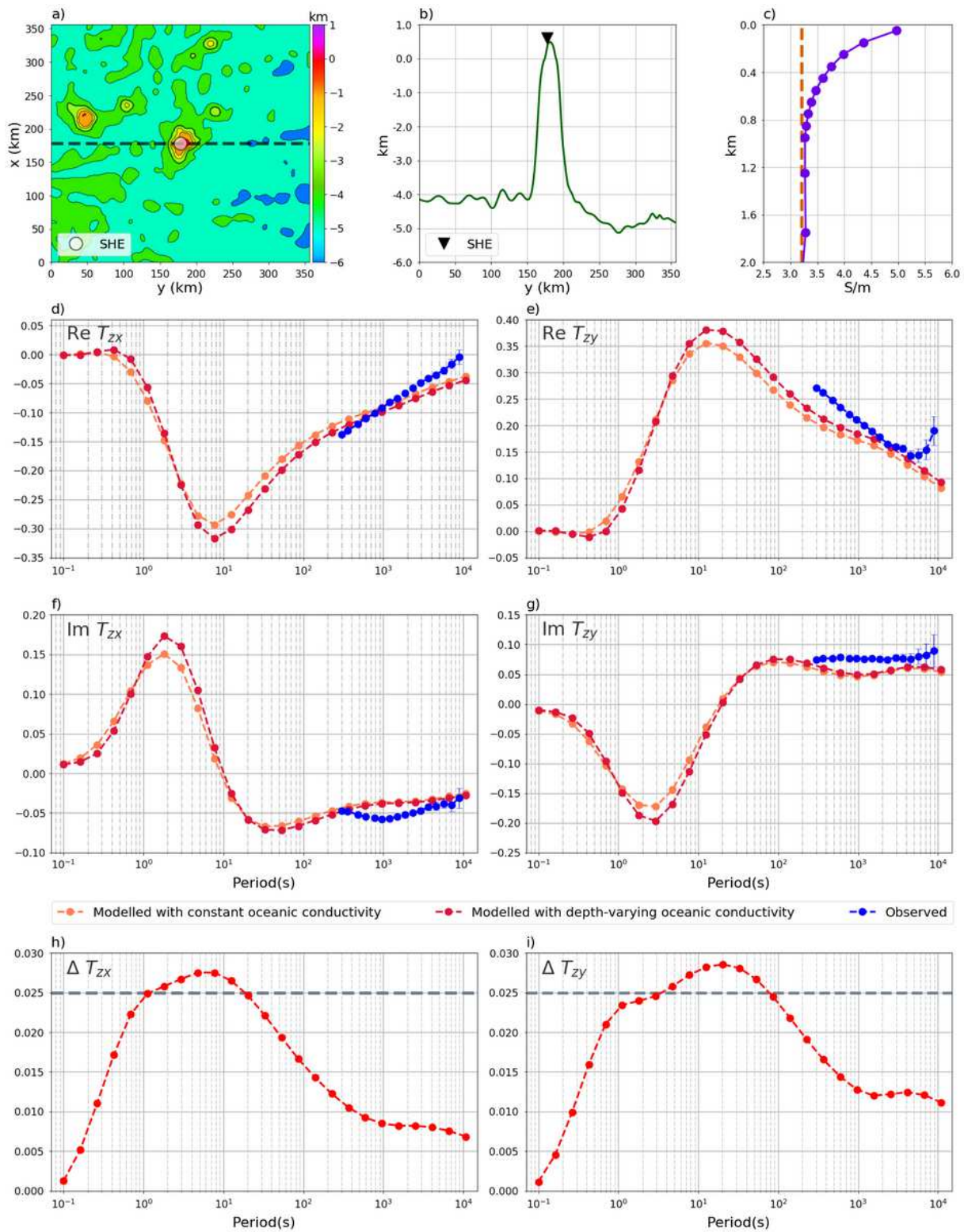


Figure 12

Same as Figure 5, but for St. Helena observatory (SHE).

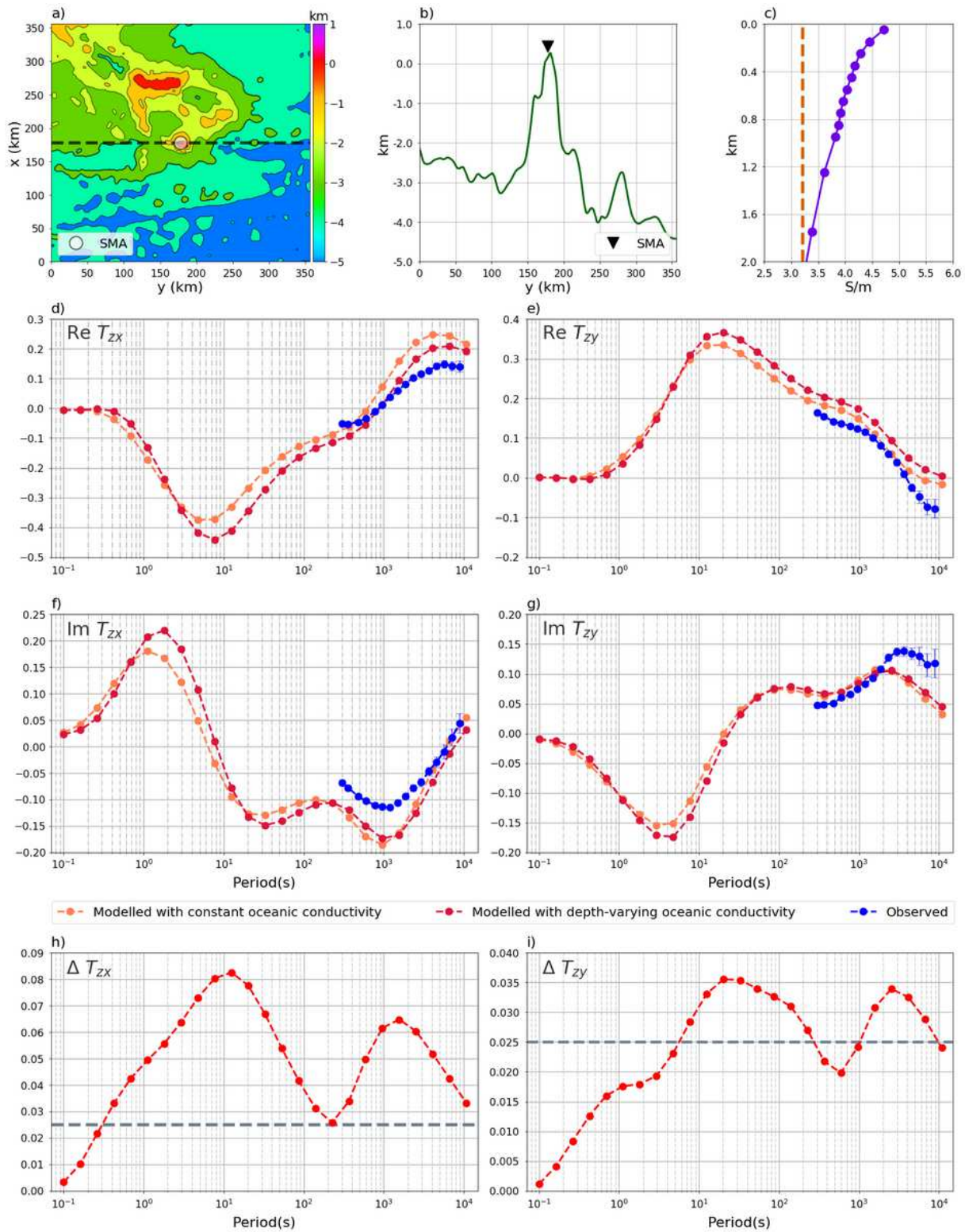


Figure 13

Same as Figure 5, but for Santa-Maria/Azores observatory (SMA).

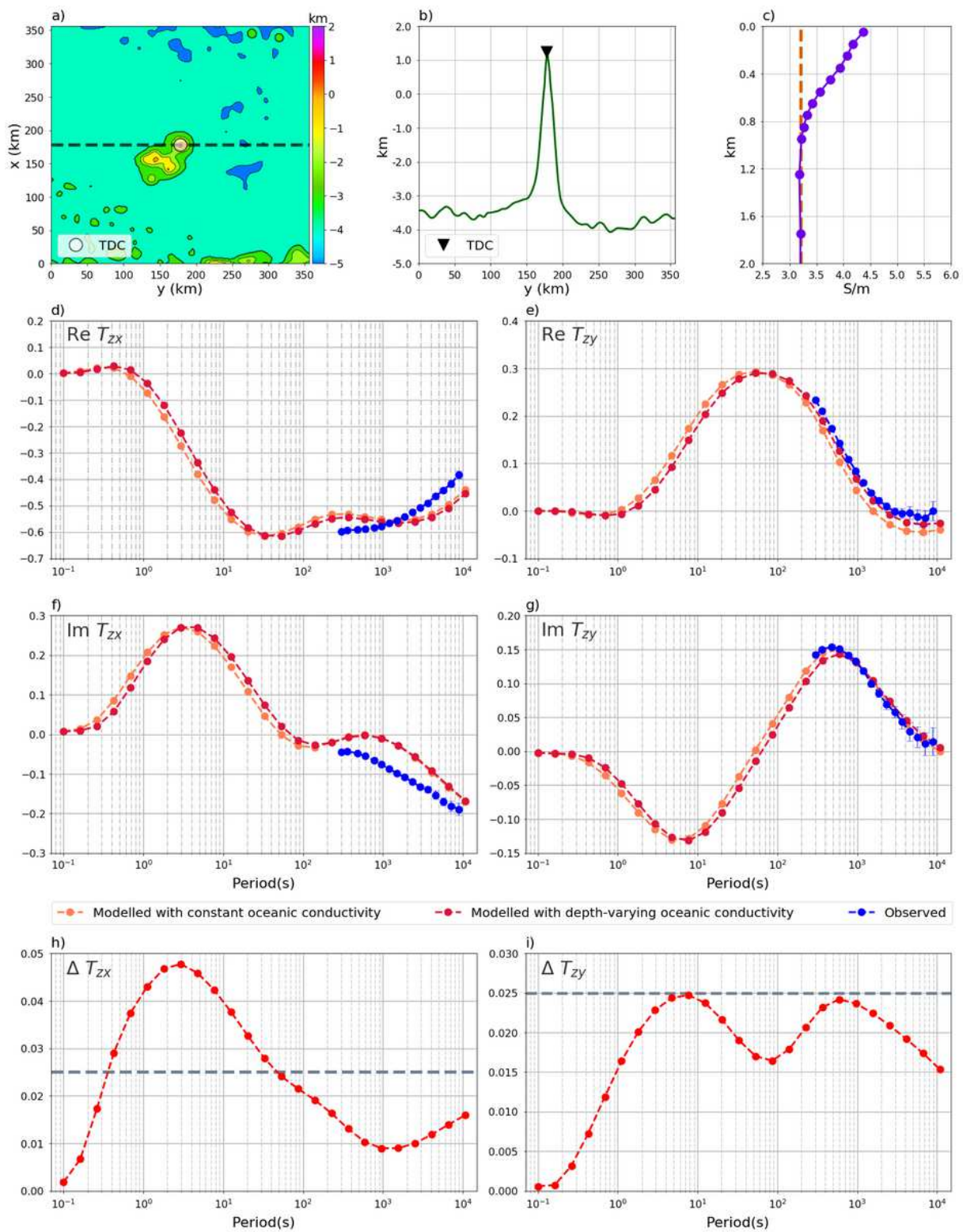


Figure 14

Same as Figure 5, but for Tristan da Cunha observatory (TDC).

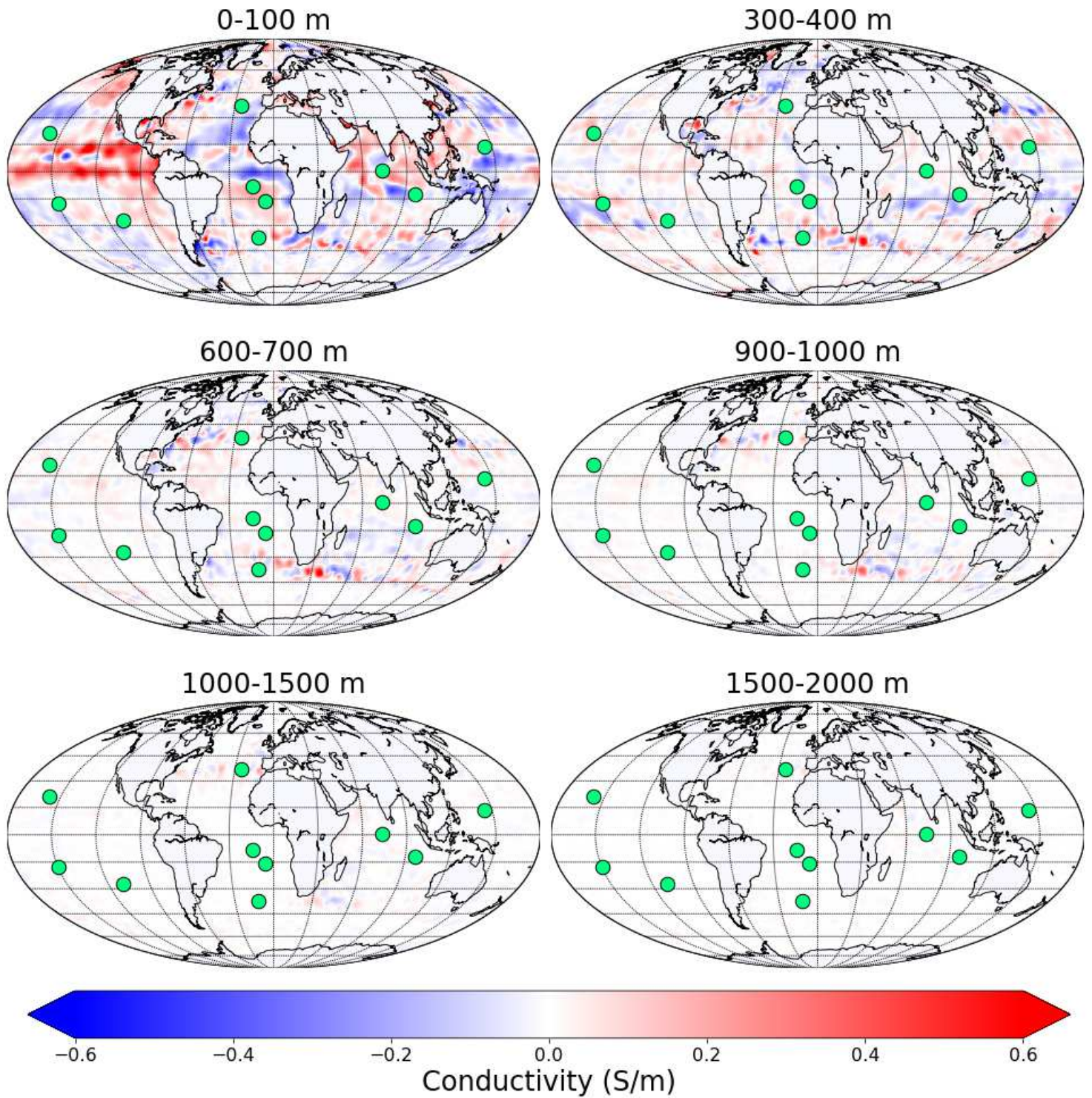


Figure 15

Global maps of difference between 2015 December and June oceanic conductivity models at six depth intervals. Green circles denote locations of geomagnetic observatories used in this study.

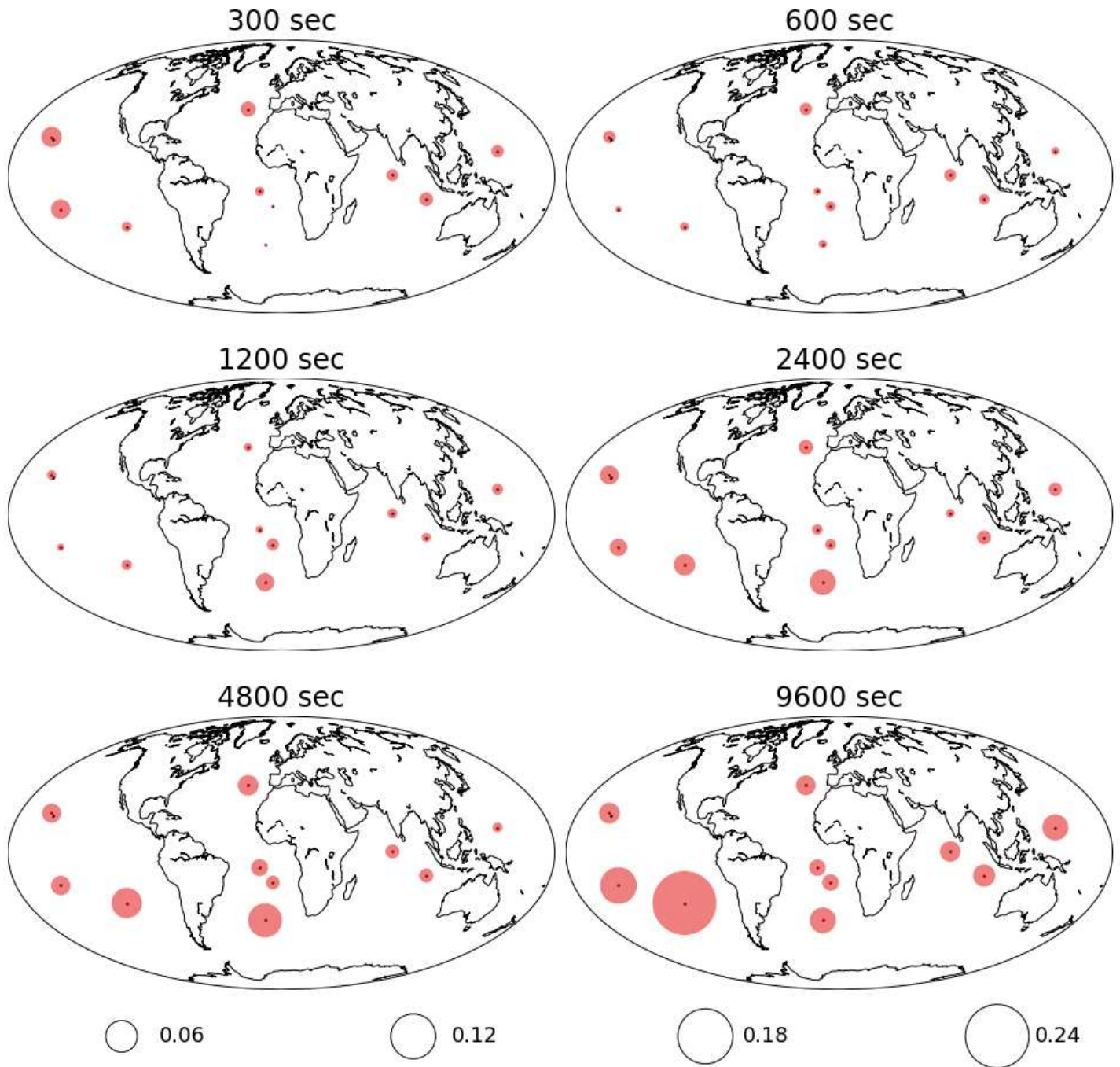


Figure 16

Difference between “December” and “June” Tzx at island observatories, shown as filled circles. “Experimental” and “modeled” differences are colored by light and dark red, respectively. The size of circles below the plots indicates four ranges of differences.

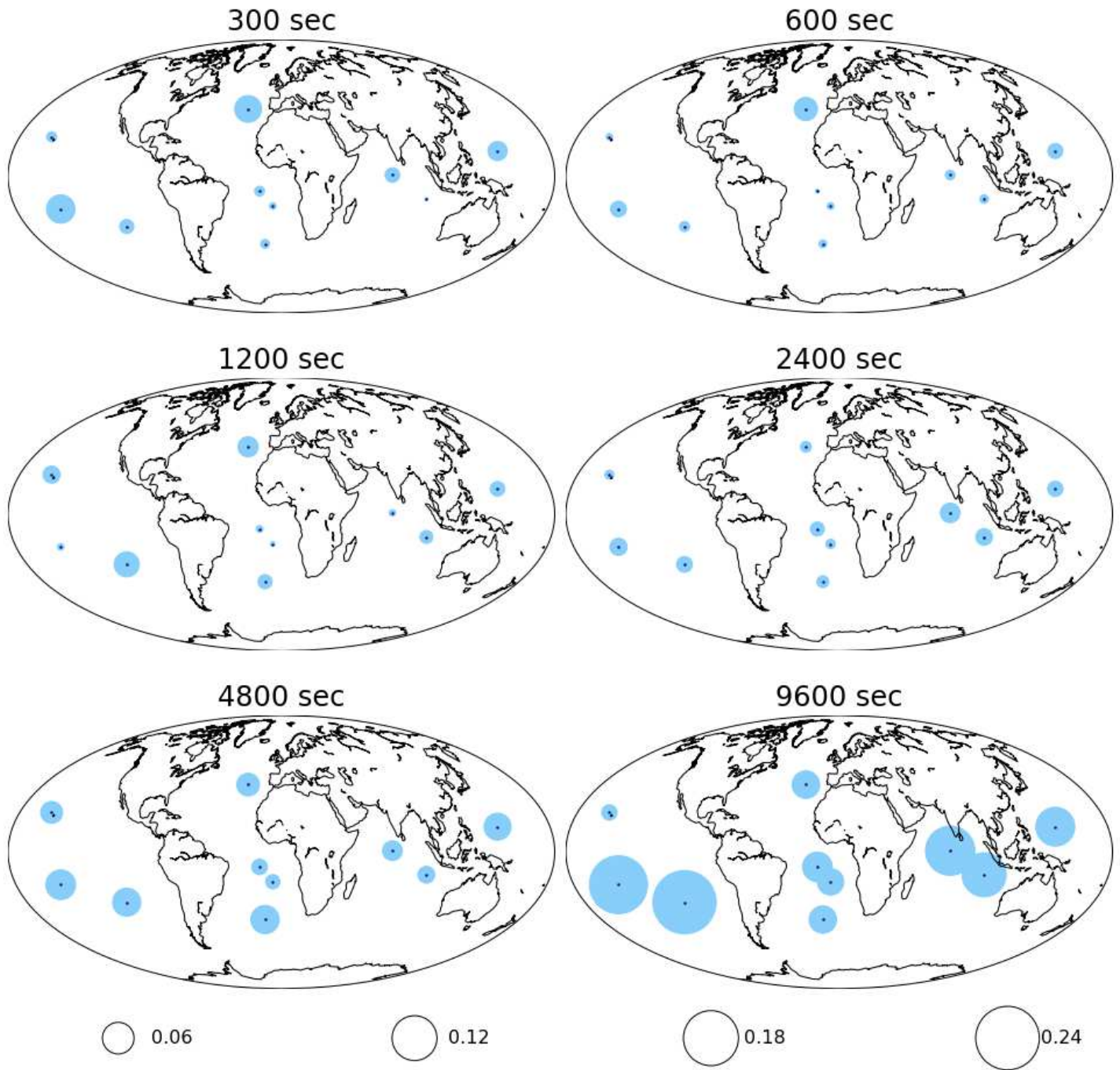


Figure 17

Same as Figure 16, but for Tzy.

Supplementary Files

This is a list of supplementary files associated with this preprint. Click to download.

- [GASubmission.png](#)